DISCLAIMER

LA-UR-25-24297

Approved for public release; distribution is unlimited.

Title:	Demonstrate new plasticity models for doped UO2 that capture dislocation mechanisms
Author(s):	Galvin, Conor Oscar; Schneider, Anton Jacques; Robbe, Pieterjan; Pachaury, Yash; Claisse, Antoine; Capolungo, Laurent; Andersson, Anders David Ragnar; Cooper, Michael William Donald
Intended for:	Report
Issued:	2025-12-12 (rev.1)

Los Alamos
NATIONAL LABORATORY

Demonstrate new plasticity models for doped UO_2 that capture dislocation mechanisms

C. O. T. Galvin[1], A. Schneider[1], P. Robbe[2], Y. Pachaury[1], A. Claisse[3], L. Capolungo[1], D. A. Andersson[1], and M. W. D. Cooper[1]

[1]*Materials Science and Technology Division, Los Alamos National Laboratory, Los Alamos, NM 87545, USA*
[2]*Sandia National Laboratories, P. O. Box 969, Livermore, 94550, CA, US*
[3]*Westinghouse Electric Sweden, Västerås SE 72163, Sweden*

April 30th, 2025

Executive Summary

In light water reactors, fuel vendors are investigating the use of dopants to modify the properties of UO_2 pellets, with the goal of improving pellet-cladding mechanical interactions during operation. Dopants are expected to 'soften' the pellets; that is, the doped pellets have higher plastic deformation than conventional UO_2. This leads to a reduction in the severity of mechanical pellet-cladding interactions, helping to reduce the hoop strain on the cladding. By minimizing the strain exerted by the pellet on the cladding, it is anticipated that cladding performance under accident conditions can be enhanced (i.e., lowering the risk of burst during a LOCA). Dopants such as chromium (Cr) promote grain growth during pellet fabrication, leading to larger grains; therefore, understanding the link between chemistry, microstructure and mechanical deformation (enhanced creep rates) behavior of UO_2 is critical to helping operators further substantiate the benefits of doping UO_2.

Historically, the nuclear energy industry has relied on empirical models to make assessments of performance. Compared to empirical models, mechanistic physics-based models provide benefits, such as, fewer data points for validation and better extrapolation where experimental data is scarce or non-existent. In this report, Bayesian inference techniques have been applied to a previously developed lower length-scale-informed diffusional creep model. The objective is to i) infer lower-length-scale parameter distributions from available experiment and then ii) determine the uncertainties in the measurable quantity (in this case creep rates) after propagating the inferred lower length scale parameter uncertainties. The approach requires many evaluations of the model, which becomes computationally insurmountable; therefore, a neural-network model is trained to data obtained by sampling the full model over the most important parameters. This neural-network is then used in the Bayesian inference approach to determine probability distributions in the parameter values that represent the uncertainty in the model given what is known from the experiments (posterior). A significant reduction compared to conservative initial (prior) uncertainties is achieved through inference against the experimental data, demonstrating the efficacy of this approach. Furthermore, by accounting for uncertainties in the experimental conditions and sample non-stoichiometry, it is possible to resolve apparent discrepancies in experimental measurements within a self-consistent grain boundary (Coble) creep model that is sensitive to chemistry. This work has been written up and submitted to Nuclear Technology for a special issue on accelerated fuel qualification (AFQ). This uncertainty quantification (UQ) work not only improves the diffusional model, while accounting for uncertainty, but also establishes a framework which can readily be applied to the mechanistic models of dislocation deformation developed in this study.

The most likely values from the Bayesian analysis are incorporated into our UO_2 diffusional creep model and a lower length scale-informed irradiation UO_2 creep mechanistic model to generate a dataset. This dataset has been provided to our INL collaborators for training an artificial neural network surrogate model, which will be implemented in the BISON fuel performance

code to assess how the results differ from those currently obtained using a fully empirical model and that of using the nominal (uncalibrated) atomic scale parameters in our mechanistic model.

Plastic deformation (creep and glide) in UO_2 is a complex phenomenon, governed by multiple underlying processes such as local defect concentrations, applied stresses, and microstructural characteristics. Consequently, there is a need for a meso-scale model with polycrystalline resolution capable of extrapolating to large grain sizes applicable to doped UO_2, where data is limited and the model can help bridge the knowledge gap. By integrating atomistic data into the polycrystal LApx code, it becomes possible to predict dislocation climb and glide plasticity that simple analytical models cannot accurately represent. The application of atomic-scale data within LApx demonstrated the importance of climb and glide mechanisms in reproducing high-stress UO_2 behavior. Behaviors such as this are crucial to capture and implement in BISON, as parts of the fuel pellet can reach temperatures where glide can occur before pellet cracking. This model which captures dislocation based mechanisms for UO_2 is then used to stand up the doped model accounting for larger grain sizes. It was found that larger grain sizes can lead to enhanced deformation rates in the glide regime, and therefore can help with the pellet cladding mechanical interaction. Therefore if the fuel pellet reaches conditions (stress/temperature) where glide is active, the enhanced creep rates for larger grains in the glide regime (doped UO_2) can help with pellet cladding mechanical interactions.

Plastic deformation in UO_2 involves multiple mechanisms, including diffusional creep, dislocation climb, and glide. This milestone contains two parts: (1) UQ of a pre-existing lower length scale informed mechanistic diffusional creep model, and (2) development of a new LApx based model for dislocation-mediated creep mechanisms in UO_2, with application to large-grain doped UO_2.

Glossary

NEAMS Nuclear Energy Advanced Modeling and Simulation
BISON Finite element-based nuclear fuel performance code
LWR Light water reactor
LOCA Loss of coolant accident
MCMC Markov Chain Monte Carlo
INL Idaho National Laboratory
LANL Los Alamos National Laboratory
AFC Advanced Fuels Campaign
AFQ Accelerated Fuels Qualification
Cr Chromium

Contents

List of Figures

1 Introduction

UO_2 has been the primary nuclear fuel for light water reactors (LWRs) for several decades. During this time, the nuclear industry has maintained a strong interest in enhancing fuel performance, driven by both economic and safety considerations. One promising approach involves doping UO_2 with elements such as chromium (Cr), which is currently being explored to modify the microstructure of the fuel and mechanical properties in order to improve its overall behavior. The introduction of Cr has been shown to promote grain growth during sintering, resulting in larger grains compared to that of undoped UO_2 [12]. The resulting large grains can positively affect fuel performance by suppressing fission gas release. Additionally, Cr doping has been shown to increase fuel creep rates [10], enhancing the viscoplastic response of the fuel. Consequently, the fuel pellet can maintain better mechanical interaction with the cladding, and, in the case of a Loss of Coolant Accident (LOCA) scenario, would reduce the likelihood of cladding failure. These examples underscore how modifications in fuel chemistry and microstructure can significantly impact performance. The potential for increased plasticity in Cr-doped UO_2 and the mechanisms driving this behavior will be the central focus of this milestone.

Among the core elements of the NEAMS program is the development of lower length scale informed mechanistic models to be implemented to the engineering scale. Compared to empirical models, mechanistic models provide benefits; for example, they require fewer data points for fitting and have better extrapolation where experimental data is scarce or non-existent. Moreover, since actual physical processes underpin mechanistic models, separate effects testing can be designed to target a subset of the model parameters, with complementing efforts coming from the AFC program using a "goal-oriented science-based approach" to provide experimental measurements.

Mechanistic models that rely on lower length scale information are often developed using atomic-scale calculations, where a meaningful uncertainty on isolated parameters is difficult to quantify from first principles [13]. Moreover, as mentioned previously, the implementation of these models in higher-level simulation codes (e.g., dislocation dynamics, cluster dynamics, phase-field simulations and crystal plasticity methods) and integrated in fuel performance codes (e.g., BISON [14]) represents a key aim of the NEAMS program. It is extremely difficult to propagate error via this multi-scale simulation approach, especially if the underpinning mechanistic models do not provide uncertainty. However, through the application of Bayesian techniques, it is possible to apply uncertainty quantification across the different models, as well as to infer the noise-level in the combined uncertainty from measurement variability and potential biases in the model, and the ability of the model to describe that scatter in a manner that is consistent with the model form and inferred parameter uncertainties.

In our previous work [11, 15, 16], a lower length scale mechanistic diffusional creep model for UO_2 was developed. A significant driving factor for developing this model was the lack of consensus for the dominant diffusional creep mechanism, i.e., Nabarro-Herring (bulk) or Coble

(grain boundary), which have different grain size dependencies (impacting their contribution to large-grain doped UO_2). Lower length-scale simulations were used to inform a validated mechanistic creep model, which conclusively showed that Coble creep mechanism is dominant and was in the correct order of magnitude compared to experimental measurements showing good agreement with experimental data across a range of conditions [2–4, 6, 7, 17–25]. Furthermore it laid the groundwork for an irradiation creep model [26] and to explore the impact of dopants [11]. One objective of the work here is to use Bayesian techniques to investigate the lack of information surrounding experimental conditions and inaccuracies in the underlying atomic-scale parameters of the model, which can be corrected through inference resulting in posterior distributions in the parameter sets. Developing the UQ framework will not only improve the diffusional creep model and incorporate uncertainties, but also establishes a foundation that can be readily applied to the dislocation model in this work, thereby facilitate future work plans.

We also examine the impact of other possible mechanisms that could yield higher creep rates for doped UO_2, including climb-limited dislocation creep and glide. Based on the work completed during last year's milestone [11], we have ruled out diffusional creep as the primary mechanism responsible for the increased plastic deformation observed in doped UO_2. We apply our atomistic predictions beyond an analytical model, extending them to polycrystalline UO_2. This is done using a chemo-mechanically coupled defect diffusion model within an elasto-visco-plastic fast Fourier transform (EVPFFT) framework [27]. This model, implemented in the LApx code, tracks the local evolution of point defects and their influence on the material's diffusion-driven plastic response. It also incorporates plasticity from dislocation climb and climb-assisted glide, capturing their effects on the mechanical behavior of the polycrystal. By integrating our latest atomistic data into this model, we can investigate mechanisms such as dislocation climb and glide, especially under conditions of high stress or large grain sizes and validate against available experimental data, including those from the AFC program. More importantly, this framework allows us to explore additional microstructural processes that may explain the enhanced plastic deformation observed in Cr-doped UO_2 fuel.

In this milestone, we expand upon our previous work [11,16] to accomplish the following objectives: (i) quantify the uncertainty in our lower length scale UO_2 diffusional creep mechanistic model using a Bayesian uncertainty quantification (UQ) framework; (ii) use the most probable values from the Bayesian calibration to update the creep model including the incorporation of an irradiation mechanistic model that accounts for the effects of fission rate - preparing it for implementation into BISON; and (iii) develop a model of dislocation climb and glide mechanisms in UO_2 using a lower length scale informed viscoplastic framework. This model is extended to stand up a baseline Cr-doped UO_2 creep model, that can provide predictions for simulations of larger grains. Enhanced glide is predicted for large grains, which shows that there is a stress regime where deformation is higher for doped UO_2. These types of behaviors are crucial to capture and implement in BISON as parts of the fuel pellet can reach temperatures and stress where glide occurs before pellet cracking. Therefore, for larger grains (doped UO_2) in the glide regime can enhance creep rates which can help with pellet cladding mechanical interactions.

2 Methods

This section discusses the lower length scale mechanistic models and the uncertainty quantification (UQ) framework. It also provides an overview and parameterization of the LApx polycrystal code.

2.1 Atomic-scale-informed models

Before jumping into the uncertainty quantification methodology, the mechanistic creep model and the atomic-scale data used to inform it need to be described. First, mechanistic models describing fuel deviation from stoichiometry, and the uranium self-diffusivity within bulk UO_2, both of which are influenced by the oxygen partial pressure, p_{O_2}, are presented. Following this, the diffusional creep model is discussed. Steady-state creep describes the plastic relaxation that a material experiences as it is subjected to a deviatoric stress at moderate to elevated temperatures. UO_2 creep can be accommodated by different deformation modes (e.g., climb, diffusional and glide) depending on local conditions and micro-structure. The analytical creep model considered for the UQ part of this report focuses on the diffusional regime only [16]. Diffusional creep has two main contributions: bulk diffusion (Nabarro-Herring [28,29]) and grain boundary diffusion (Coble [30]), both of which have different grain size dependencies. In terms of nuclear fuel performance, pellet creep impacts the closure rate of the pellet-cladding gap and then, following closure, the mechanical strain imparted on the cladding by the pellet. Therefore, uncertainty in the creep model translates to uncertainty in the stress-state of the cladding as a function of burnup. This creates uncertainty in, for example, predictions of cladding ballooning and rupture during a loss of coolant accident (LOCA). Although these models (non-stoichiometry, self-diffusivity and creep) describe different phenomena, they are inter-connected through several common underlying parameters. Hence, by considering calibration of these models (along with their common parameters) across the available creep, single crystal self-diffusivity and non-stoichiometry experimental measurements, the joint combined probability distribution of all uncertain parameters in the models can be inferred and the overall uncertainty can be reduced.

2.1.1 Non-stoichiometry

In the models outlined below, UO_2 non-stoichiometry (i.e., x in $UO_{2\pm x}$) is calculated as a function of temperature and p_{O_2}, and taken into consideration. The defect chemistry controls the non-stoichiometry, which impacts the concentration of point defects, and therefore, bulk uranium self-diffusion. This also impacts the creep rates as bulk point defects are used as an input to predict the defect concentrations at the grain boundary, a key input for Coble creep rates (see the studies by Galvin et al. [16] and Neilson et al. [26] for more details). A necessary constraint

when calibrating the full model is to have experimental thermodynamic data of $UO_{2\pm x}$ non-stoichiometry, with temperature and p_{O_2} as inputs. This enables calibration of $H_{fp_{O_2}}$ and T_0 (see section 2.1.3), which capture the temperature dependence of p_{O_2} in experiments as governed by the environmental conditions, while obtaining reasonable non-stoichiometries, and without wildly varying bulk lattice defect energies to compensate. This thermodynamic constraint was also implemented in a previous study for the calibration of Xe diffusion in UO_2 [9].

2.1.2 Uranium self-diffusivity

The uranium self-diffusivity in the bulk UO_2 lattice can be predicted as a function of temperature and p_{O_2} [16, 31, 32] under thermal equilibrium conditions. The formation energies of intrinsic point defects in bulk UO_2 were estimated to predict concentrations using the method of Dorado et al. [31], formulated to relate defect concentrations to density functional theory-obtained point defect formation energies that describe the interaction of atoms, interstitials, and vacancies in $UO_{2\pm x}$ with an external reservoir of oxygen atoms. Whilst uranium vacancies are the defect of interest, it is important to note that, in UO_2, their concentration is coupled to the thermochemistry of the UO_2 system, which is accounted for in these models. In order to predict the diffusion coefficients, density functional theory migration barriers and empirical potential calculated attempt frequencies given in [32, 33] were used. This model has been calibrated previously by Robbe et al. [9]. Similarly, the predicted uranium self-diffusivity of UO_2 and the single crystal experimental measurements from Sabioni [8] are included here to add additional constraints while calibrating the underlying bulk defect energy parameters, along with $H_{fp_{O_2}}$ and T_0.

2.1.3 Diffusional creep rates

Numerous studies have been conducted on UO_2 creep rates, but, despite this, there is disagreement as to what the dominant diffusional creep mechanism is. To address this, a mechanistic diffusional creep model informed by atomic-scale simulations was previously developed under the NEAMS program for UO_2 [16], at thermal equilibrium, where stress, grain size, temperature and p_{O_2} are accounted for. It was found that Coble creep is the dominant mechanism in the diffusional regime [16], and that the creep rates are governed by the self-diffusion of uranium vacancies at the grain boundary. Nabarro-Herring creep, controlled by bulk diffusion, was shown to predict creep rates many orders of magnitude too low to describe the experimental measurements [16], which eliminated it as a possible mechanisms even with conservative prior uncertainties. In addition the bulk diffusivity data by Sabioni et al. [8] confirmed that these bulk values are accurate [16]. Possessing this information, the mechanistic-informed creep model calibrated in this study is based off the analytical Coble equation [16, 30, 34, 35, 51] with a nucleation rate limited term accounting for the lack of grain boundary dislocations to mediate creep at low stresses. Under thermal equilibrium conditions, uranium vacancies and not uranium interstitials had the dominant impact, see [16, 26]. The model expression is given by:

$$\dot{\varepsilon}_{Coble} = \frac{42|\Omega_{V_{U,GB}}|D_{V_U}^{GB}[V_{U,GB}]\pi\delta}{k_B T G^3}\sigma_v \left(\frac{\dot{N}^2}{\dot{N}^2 + \frac{1}{2}}\right), \tag{2.1}$$

where $\dot{N}$ is a normalized grain boundary dislocation nucleation rate, which is a term that accounts for the fact that there are local regions of stress (such as at triple junctions) that are higher relative to the applied stress and that this enables nucleation of dislocations. $\dot{N}$ contains stress, grain size, and temperatures dependencies that are described in more detail in [51]. $[V_{U,GB}]$ is the uranium vacancy concentration at the grain boundary, $\Omega_{V_{U,GB}}$ is the uranium vacancy defect volume at the grain boundary, $D_{V_U}^{GB}$ is the diffusivity of a uranium vacancy at the grain boundary (calculated from atomistic data and are given in previous studies [16,26]), δ is the grain boundary thickness, T is temperature, σ_v is the von-Mises stress, k_B is the Boltzmann constant, and G is the grain size. The uranium vacancy concentrations at grain boundaries are dependent on the oxygen partial pressure (p_{O_2}) of the system. In this work, the temperature-dependence of p_{O_2} [16, 31, 32] is predicted and described by assuming oxygen partial pressure is buffered by an oxygen reaction [32]. Of the creep experiments used for calibration, only three provided details about the testing environment: one was conducted under a CO_2 environment [3] and two were under a H_2 environment [1,4]. For the remainder [5–7,17], we do not have the conditions, therefore, we set a large prior uncertainty, see Appendix A2. A model that describes the temperature dependence of p_{O_2} [32] is employed, where $H_{fp_{O_2}}$ denotes the enthalpy for the reaction controlling the oxygen potential, and T_0 is the temperature at which UO_2 is regarded as stoichiometric for the given value of $H_{fp_{O_2}}$ (equation 34 in [32]). Bulk defect energies are dependent on p_{O_2}, which in turn impact the grain boundary defect concentration, through defect equilibrium and the segregation energy, and consequently the creep rates. More detailed information on this can be found in [16].

2.2 Uncertainty quantification

Given the defined mechanistic models, what follows is the description for the Bayesian calibration methodology leveraged for uncertainty quantification. The atomistic-scale models are formalized as follows; the model describing creep rates is denoted as $C(\boldsymbol{\nu};\boldsymbol{x})$, where $\boldsymbol{\nu}$ are the underlying atomic-scale parameters that need to be estimated, and $\boldsymbol{x}$ are the independent variables (T, G, σ_v, and p_{O_2}). Similarly, the model for uranium self-diffusivity is denoted as $D(\boldsymbol{\nu};\boldsymbol{x})$ and the model for non-stoichiometry as $S(\boldsymbol{\nu};\boldsymbol{x})$.

2.2.1 Bayesian inference

In the Bayesian setting, the atomistic-scale parameters are modeled as random variables with a prescribed prior distribution $p(\boldsymbol{\nu})$. Here, the assumption is that the parameters are uniformly distributed between a given lower and upper bound that are determined by prior experience based on familiarity with typical errors present in atomistic calculations.

The goal of Bayesian inference is to approximate the so-called posterior distribution $p(\boldsymbol{\nu}|\mathcal{D})$, i.e., the distribution of the parameters after observing the data $\mathcal{D}$. In this context, the data corresponds to the measurements in the different experiments discussed in section 2.1. Each experiment is split into different measurement groups, where measurements performed at the same temperature and with the same grain size are grouped together. These measurement groups are denoted as $\mathcal{D} \coloneqq \{\mathcal{D}_j\}_{j\in\mathcal{J}}$ where $\mathcal{J}$ is the collective set of measurement groups across all experiments, see 2.1. Each of these measurement groups consists of a set of measurements

$\mathcal{D}_j \coloneqq \{\boldsymbol{x}_j^{(i)}, y_j^{(i)}\}_{i=1}^{N_j}$, where $\boldsymbol{x}_j^{(i)}$ is the measurement location for the ith measurement in measurement group j, $y_j^{(i)}$ is the value of the measurement, and N_j is the number of measurements in measurement group j.

Table 2.1: List of experiments considered in this work [1–7, 17] and those contained within [9]. For each experiment, the predicted quantity, the total number of measurements in the experiment, and the number of measurement groups are listed. Note that the experimental creep data has been filtered to only include data in the diffusional regime. Burton & Reynolds[1] and Burton & Reynolds[2] refer to two separate experiments, [4] and [3], respectively.

Experiment	Predicted quantity	# measurements	# measurement groups
Armstrong	Creep rate	18	4
Bohaboy	Creep rate	32	12
Burton & Reynolds[1]	Creep rate	28	3
Burton & Reynolds[2]	Creep rate	14	2
Kaufman	Creep rate	6	2
Seltzer	Creep rate	5	1
Chung & Davies	Creep rate	39	5
Sabioni	U self-diffusivity	10	1
Various studies	Non-stoichiometry	104	1
Total	-	256	31

Let $z_j^{(i)}(\boldsymbol{\nu}) \coloneqq P_j(\boldsymbol{\nu}; \boldsymbol{x}_j^{(i)})$ be the model response for the ith measurement in measurement group j, with $P_j \in \{C, D, S\}$ the predicted quantity in measurement group j. It is assumed that the measurements correspond to noisy model outputs according to the data model

$$y_j^{(i)} = z_j^{(i)} + \sigma_j \xi_j^{(i)}, \quad i = 1, \ldots, N_j, \tag{2.2}$$

where $\xi \sim \mathcal{N}(0,1)$ is a standard normal random variable and σ_j is the standard deviation of the uncertainty due to measurement noise and model discrepancy for measurement group j. These standard deviations will be inferred from the data along with the other model parameters. Bayes' theorem relates the posterior to the prior as

$$p(\boldsymbol{\nu}|\mathcal{D}) \propto \mathcal{L}_{\mathcal{D}}(\boldsymbol{\nu}) p(\boldsymbol{\nu}), \tag{2.3}$$

where $\mathcal{L}_{\mathcal{D}}(\boldsymbol{\nu})$ is the likelihood of observing the parameters $\mathcal{D}$ given the data $\boldsymbol{\nu}$. For the Gaussian data model in Equation (2.2), the (log of the) likelihood can be written explicitly as

$$\log \mathcal{L}_{\mathcal{D}}(\boldsymbol{\nu}) = \sum_{j \in \mathcal{J}} \mathcal{L}_{\mathcal{D}_j}(\boldsymbol{\nu}),$$

where

$$\log \mathcal{L}_{\mathcal{D}_j}(\boldsymbol{\nu}) = -\frac{N_j}{2} \log(2\pi\sigma_j^2) - \frac{1}{2\sigma_j} \sum_{i=1}^{N_j} \left(y_j^{(i)} - z_j^{(i)}(\boldsymbol{\nu}) \right)^2. \tag{2.4}$$

To sample from the posterior distribution $p(\boldsymbol{\nu}|\mathcal{D})$, Markov Chain Monte Carlo (MCMC) is used. Specifically, the adaptive MCMC algorithm from Haario et al. [36] is employed. This method relies on repeated sampling of the right-hand side of Equation (2.3) using an acceptance-rejection scheme with a tunable proposal distribution based on past samples during the sampling process. Refer to [37] for more details.

For computational efficiency reasons, Equation (2.4) is not used directly in the Bayesian inference setup. Instead, two approximations are made. First, because Bayesian calibration in a high-dimensional setting (i.e., a large number of parameters) is challenging, a sensitivity analysis is performed prior to the inference in order to reduce the number of atomic-scale parameters to estimate. Second, because model evaluations $z_j^{(i)}$ are computationally expensive, they will be approximated using a cheaper-to-evaluate surrogate model. These two approximations are discussed for the remainder of this section.

2.2.2 Dimension reduction through sensitivity analysis

Following the exposition in [9], a global sensitivity analysis (GSA) is performed to identify a reduced set of atomistic parameters. The sensitivity analysis ranks parameters according to their relative effect on the variance of the output (variance-based sensitivity analysis), allowing a down-selection based on the fractional contribution of each parameter to the total output variance. To this end, the so-called total-effect Sobol' sensitivity indices are computed. These indices capture the effect of each parameter on the output variance, including the effects caused by interactions with other parameters. Sobol' indices can easily be computed from a polynomial chaos expansion (PCE) approximation for the model during a post-processing step, see [38].

A PCE for the model response $z_j^{(i)}(\boldsymbol{\nu})$ can be written as equation 2.5

$$z_j^{(i)}(\boldsymbol{\nu}) \approx \sum_{k=1}^{K} c_{k,j}^{(i)} \Psi_k(\phi(\boldsymbol{\nu})), \tag{2.5}$$

where Ψ_k is a multivariate orthogonal polynomial, $c_{k,j}^{(i)}$ is a deterministic coefficient that needs to be determined, and K is the number of coefficients in the expansion [39]. In case of uniformly distributed input parameters $\boldsymbol{\nu}$, as is the case here, the polynomials Ψ_k are the normalized Legendre orthogonal polynomials, and the mapping ϕ represents a linear scaling from the input space to $[-1,1]^d$, the support of the polynomials. The coefficients $c_{k,j}^{(i)}$ are estimated from a training set of input-output evaluations

$$\mathcal{Z}_j^{(i)} = \{(\boldsymbol{\nu}^{(m)}, z_j^{(i)}(\boldsymbol{\nu}^{(m)}))\}_{m=1}^{M}, \tag{2.6}$$

where M is the number of samples, drawn randomly from the prior distribution $p(\boldsymbol{\nu})$. The sought-after Sobol' sensitivity indices can then be computed by combining the appropriate coefficients from the expansion, see [9, equation (10)].

Finally, adding the sensitivity contributions of each parameter across the different measurements allows a ranking of the parameters according to their overall importance. In particular, the parameters can be split out into a set of important parameters $\boldsymbol{\nu}_r$ and a set of less important

parameters $\boldsymbol{\nu}_{-r}$ where $\boldsymbol{\nu} = \boldsymbol{\nu}_r \cup \boldsymbol{\nu}_{-r}$. In the results presented later, only a reduced set of 14 parameters $\boldsymbol{\nu}_r$ are retained, and the remaining parameters $\boldsymbol{\nu}_{-r}$ are fixed to their nominal values. This reduced set of parameters was identified by applying a 99% threshold to the fraction of explained variance.

2.2.3 Surrogate construction

In [9], polynomial surrogate models constructed for sensitivity analysis were retained for the subsequent calibration. However, because these surrogates only had limited point-wise accuracy for prediction, there was still a remaining discrepancy between the surrogate model and the actual model when evaluated at the inferred model parameters, see [9, Figure 13]. In an effort to alleviate this error, a neural network (NN) surrogate with improved point-wise prediction accuracy is used here.

The surrogate model employs a multi-head architecture with shared feature extraction layers. The network consists of four shared fully connected layers followed by three parallel output heads, each specialized for different physical properties (creep, diffusivity, and non-stoichiometry).

The 4 fully connected shared layers comprise first 64, then 128, 256 and finally 512 neurons. All shared layers use ReLU activation functions [40]. These layers learn common feature representations across all output variables.

The training data set contains 500,000 input-output pairs, sampled from the prior distribution of the reduced parameter set, with all remaining parameters held at their nominal values. To address data imbalance across output values, stratified sampling is applied. Each output variable was divided into 10 equal-sized strata based on its output range. From each stratum, 5,000 samples were randomly selected, forming a balanced data set of approximately 100,000 points. For training and evaluation, this data set is partitioned by withholding 20% for testing and reserving 25% of the remaining data for validation. A logarithmic transformation in base 10 is applied to the creep and diffusivity data, but the raw output values for the non-stoichiometry data are retained.

The network was trained for 10,000 epochs using the Adam optimizer [41] with an initial learning rate of 0.001 and mean squared error loss. A learning rate scheduler was introduced to reduce the learning rate by a factor of 10 if no improvement in the validation loss was observed over 50 consecutive epochs. Additionally, a patience of 100 was used, designating the number of epochs the training must go through before stopping after reaching a validation loss minimum. The best state achieved yields a validation loss of 0.0059 using a mean squared error loss function.

2.3 Dislocation plasticity modeling (LAPx simulations)

LApx is a full-field FFT-based solver that models the thermo-mechanical behavior of polycrystalline materials under extreme environments, capturing complex multiphysics phenomena like creep, fatigue, and damage. It supports anisotropic elasticity/plasticity, and easily integrates advanced constitutive models for predicting material response under complex loading. An in-

depth description of the LApx code can be found in [42], here we provide an overview of the main mechanisms. The continuum-level crystal plasticity framework is based on small-strain kinematics, where the total strain rate, $\dot{\varepsilon}$, is additively decomposed into elastic, $\dot{\varepsilon}^{el}$, and plastic, $\dot{\varepsilon}^{p}$, strain rates, given by equation 2.7,

$$\dot{\varepsilon}_{ij} = \dot{\varepsilon}^{el}_{ij} + \dot{\varepsilon}^{p}_{ij} \tag{2.7}$$

The total plastic strain rate, equation 2.8, is given by the additive contributions from vacancy diffusion, dislocation climb, and dislocation glide,

$$\dot{\varepsilon}^{p}_{ij} = \dot{\varepsilon}^{dif}_{ij} + \dot{\varepsilon}^{cl}_{ij} + \dot{\varepsilon}^{dis}_{ij} \tag{2.8}$$

For the LApx simulations in this report we omit $\dot{\varepsilon}^{dif}_{ij}$ since a mechanistic diffusional model is already employed (see section 2.1.3) and our focus here is on the contributions from dislocation climb and glide. The total creep rate can then be obtained by summing the diffusional model's output with the climb and glide components from LApx. These regimes are also identified as the most important for Cr-doped UO_2 [10]. Plastic relaxation via dislocation climb occurs only in the bulk and is considered only for edge dislocations. The strain rate due to dislocation climb, equations 2.9 and 2.10 thus depends on the local edge dislocation density in dislocation cells, $\rho^{s}_{cell,edge}$, and the climb velocity, v^{s}_{climb}, for the different slip systems, $s = 1, \ldots, S$, where S is the total number of active slip systems:

$$\dot{\varepsilon}^{climb}_{ij} = \sum_{s=1}^{S} l^{s}_{ij} \bar{\dot{\beta}}^{s} \tag{2.9}$$

$$\bar{\dot{\beta}}^{s} = c_r \rho^{s}_{cell,edge} b^{s} v^{s}_{climb} \tag{2.10}$$

Here, c_r is the climb reduction ratio, b^s is the magnitude of the Burgers vector, and l^{s}_{ij} is the climb tensor, defined as $l^{s}_{ij} = b^{s} \otimes b^{s}$ for edge dislocations only [43]. $\rho^{s}_{cell,edge}$ denotes the edge dislocation density, and v^{s}_{climb} represents the climb velocity, which depends on the net flux of point defects to and from the dislocation, given by equation 2.11:

$$v^{s}_{climb} = \frac{\Omega}{b^{s}} D^{bulk} z^{s}_{v} \left(c^{core}_{v} - c^{bulk}_{v} \right) \tag{2.11}$$

In this expression, D^{bulk} and z^{s}_{v} represent the bulk vacancy diffusivity and the vacancy capture efficiency of the dislocation, respectively [44, 45]. c^{core}_{v} and c^{bulk}_{v} are the vacancy concentrations at the dislocation core and in the surrounding bulk, respectively, see equations 2.12 and 2.13. The vacancy concentration at the dislocation core depends on the local stress and temperature and is given by:

$$c^{core}_{v} = c^{bulk}_{v} \exp\left(\frac{\Omega \tau^{s}_{climb}}{kT} \right) \quad \text{[42].} \tag{2.12}$$

Here, τ^{s}_{climb} is the Piola-Kirchhoff force for climb. The thermal equilibrium vacancy number concentration (site fraction) in the bulk is generally expressed as:

$$c^{bulk}_{v} = \frac{n}{N} = \exp\left(\frac{s_f}{k} \right) \exp\left(\frac{-E_f}{kT} \right) \tag{2.13}$$

where E_f and s_f refer to the vacancy formation energy and entropy, respectively. The n and N correspond to the number of vacancies and the number of atoms at lattice sites, respectively.

The dislocation glide model follows directly from [43].The shear deformation from dislocation glide is due to the combined shear rate from dislocation slip in the different slip systems, under the imposed resolved shear stress, τ^s, given by equations 2.14 and 2.15:

$$\dot{\varepsilon}^{dis} = \sum_s m_{ij}^s \dot{\gamma}^s \tag{2.14}$$

$$\dot{\gamma}^s = \rho_{cell}^s b^s v^s \text{sign}(\tau^s) \tag{2.15}$$

where, ρ_{cell}^s, v^s are the cell dislocation density and mean dislocation velocity for the different slip systems. m_{ij}^s is the symmetric part of the Schmid tensor for the different slip systems, and, $\text{sign}(\tau^s)$ enforces the direction of shear rate to be the same as the direction of glide [43]. The Hall-Petch relation is a contribution in the computation the critical resolved shear stress, where the strengthening contribution is proportional to the shear modulus and Burgers vector, and inversely proportional to the square root of the grain diameter. For a full detailed description of the model refer to [42]. For the simulations, a micro-structure with $32\times32\times32$ voxels are used. Other important parameters used are outlined in table 2.2 (more details of the LApx code can be found in [42]).

Table 2.2: Material parameters for UO_2 LApx creep simulations at 1623K. When values are listed more than once, they correspond to different slip modes.

Parameter Name	**Symbol**	**Value**	**Unit**
Atomic Volume	Ω	8.6×10^{-30}	m^3
Grain Boundary Width	δ_{gb}	1.0	nm
Bulk Diffusion Prefactor	D_0^{bulk}	4.2×10^{-7}	$m^2\,s^{-1}$
Bulk Migration Energy	E_m^{bulk}	4.233	eV
Bulk Formation Energy	E_f^{bulk}	1.3	eV
Activation Energy Dislocation	ΔG_0	5.22 – 5.71	eV
Dislocation Cell Density	ρ_{cell}^s	1×10^{11} – 1×10^{11}	m^{-2}
Rate Sensitivity Exponent	p	0.7 – 0.7	–
Regularization Exponent	q	1.3 – 1.3	–
CRSS Superposition Exponent	n	2.2 – 2.2	–
Elastic Constant	C_{11}	297	GPa
Elastic Constant	C_{12}	97	GPa
Elastic Constant	C_{44}	57	GPa

From our previous work [11], pipe diffusion at dislocation cores is shown to have an impact. Therefore, to account for this an effective diffusivity in UO_2 considering bulk and dislocation (pipe) diffusion is given by:

$$D_{\text{eff}} = D_{\text{bulk}} + fD_{\text{pipe}}$$

where $f = 10^{-4}$ is a a dislocation contribution fraction (constant), estimated as the cross section of a dislocation multiplied by a dislocation density of 1×10^{14}. Using given parameters:

$$D_{0,\text{bulk}} = 1\times10^{-7}\,\text{m}^2/\text{s}, \quad Q_{\text{bulk}} = 4.7\,\text{eV}$$

$$D_{0,\text{pipe}} = 1\times10^{-2}\,\text{m}^2/\text{s}, \quad Q_{\text{pipe}} = 1.82\,\text{eV}$$

$D_{bulk} << fD_{pipe}$ from 1000-2000 K.

Table 2.3: Strength parameter τ_0 for different slip modes, from the plot in [46]

Parameter	**Slip Mode**	**Values**
τ_0	Mode 1	Temperatures (K): 600, 1000, 1200, 1600, 2000 τ_0 (MPa): 70, 60, 40, 22, 18
	Mode 2	Temperatures (K): 600, 1400, 1900, 2000 τ_0 (MPa): 150, 90, 40, 35

To capture the correct behavior of UO_2 two dominant slip systems [46–48] were added to the LApx code, that is dislocation glide in $\frac{1}{2}\langle110\rangle\{100\}$ and $\frac{1}{2}\langle110\rangle\{110\}$. These are shown in the table 2.4 below [47].

Table 2.4: Dislocation slip systems in UO_2, table recreated from [47].

Number	**Slip System I**	**Slip System II**	**Slip System III**
1	$\frac{1}{2}[011]$ on (100)	$\frac{1}{2}[011]$ on $(01\bar{1})$	$\frac{1}{2}[011]$ on $(\bar{1}1\bar{1})$, $(1\bar{1}\bar{1})$
2	$\frac{1}{2}[01\bar{1}]$ on (100)	$\frac{1}{2}[01\bar{1}]$ on (011)	$\frac{1}{2}[01\bar{1}]$ on $(1\bar{1}1)$, (111)
3	$\frac{1}{2}[101]$ on (010)	$\frac{1}{2}[101]$ on $(10\bar{1})$	$\frac{1}{2}[101]$ on $(1\bar{1}1)$, $(\bar{1}1\bar{1})$
4	$\frac{1}{2}[10\bar{1}]$ on (010)	$\frac{1}{2}[10\bar{1}]$ on (101)	$\frac{1}{2}[10\bar{1}]$ on (111), $(1\bar{1}\bar{1})$
5	$\frac{1}{2}[1\bar{1}0]$ on (001)	$\frac{1}{2}[1\bar{1}0]$ on (110)	$\frac{1}{2}[1\bar{1}0]$ on (111), $(\bar{1}1\bar{1})$
6	$\frac{1}{2}[110]$ on (001)	$\frac{1}{2}[110]$ on $(1\bar{1}0)$	$\frac{1}{2}[110]$ on $(1\bar{1}1)$, $(1\bar{1}\bar{1})$

3 Results

This section presents the results of the multi-scale modeling approaches applied to both UO_2 and Cr-doped UO_2. Firstly, an uncertainty quantification framework is carried out to infer likelihood distributions on the atomic-scale parameters used in the UO_2 diffusional creep model, while accounting for experimental uncertainties and unknowns. Second, using the most likely parameters from this, an updated data set is generated to be provided to INL for training of a reduced order model to be implemented into BISON. This includes a lower length scale informed mechanistic irradiation model which enables the extension of the dataset to lower temperatures and include the impact of fission rate. Finally, using the atomic scale data in the LApx code, a plasticity model including dislocation climb and glide mechanisms is developed for UO_2 and validated against experimental measurements. Moreover, this is extended to stand up a Cr-doped UO_2 model where predictions are compared to available experimental data.

3.1 Uncertainty quantification

3.1.1 Sensitivity analysis

Figure 3.1 shows the total-effect Sobol' sensitivity indices for each experiment, averaged over all measurements. Parameters are sorted according to their relative importance, where importance is defined as the sum of the sensitivity indices across all measurement groups. Results are based on a set of $M = 125,000$ input-output evaluations, see Equation (2.6). Applying a threshold of 99% on the total variance explained, results in a subset of 14 parameters that will be retained for inference. These parameters include:

- UO_2 bulk enthalpy of a uranium vacancy (H_{VU}), a hole (H_h), an oxygen interstitial (H_{Oi}) and a UO_2 cell (H_{UO_2}).
- entropy of an oxygen interstitial (S_{Oi}) and a UO_2 cell (S_{UO_2}).
- the grain-boundary vacancy migration barrier (H^m_{VU}), prefactor ($D_0^{VU,GB}$), and, uranium vacancy and oxygen vacancy segregation enthalpies (H^{seg}_{VU} and H^{seg}_{VO}).
- two parameters describing the temperature dependence of the activation volume [51, see ν^* in Table (1)].
- the parameters describing p_{O_2}: T_0 and H_{fpo_2}.

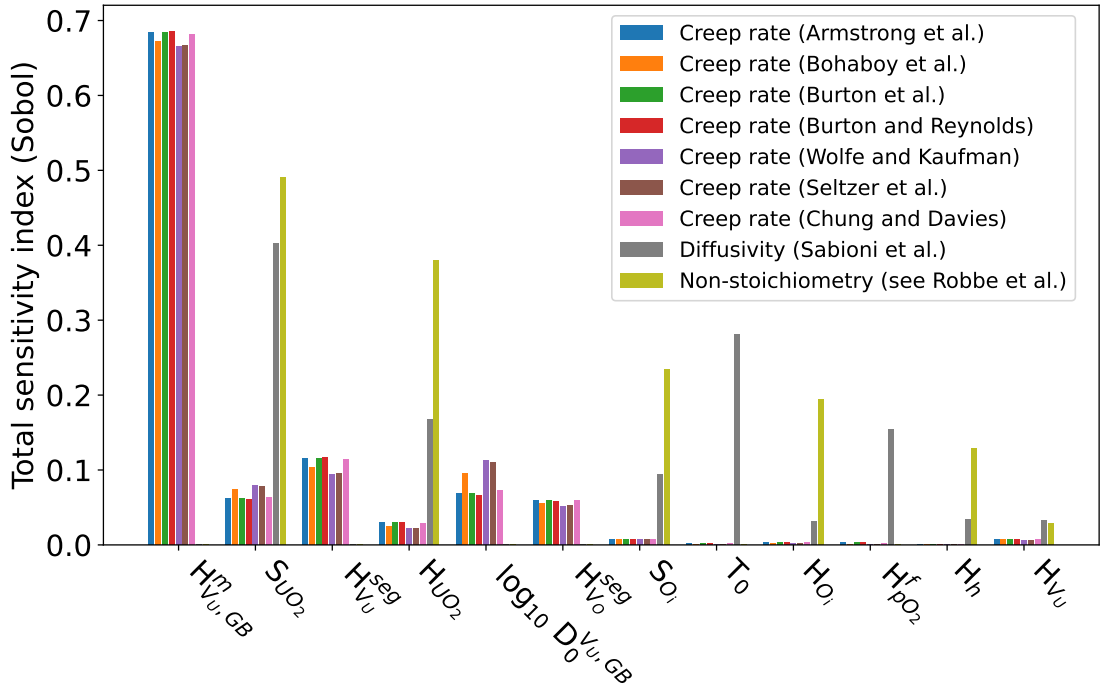

Figure 3.1: Sensitivity analysis showing most important model parameters. Armstrong [1], Burton [2–4], Kaufmann [5], Seltzer [6] and Chung and Davies [7] refer to creep rate experiments. Sabioni [8] refers to single crystal uranium self-diffusivity measurements.

The importance of these parameters makes physical sense, for example, the uranium defects at the grain boundary are rate limiting for Coble creep, and the oxygen defect segregation important for defect charge neutrality at the grain boundary (see Galvin et al. [16]). The temperature dependence of the activation volume is essential to describe low stress and low temperature creep rates (see Dillon et al. [51]). The enthalpies and entropies (H_{VU}, H_h, H_{Oi}, H_{UO_2} S_{Oi} and S_{UO_2}) are crucial parameters in determining formation energies, which in turn affect bulk defect concentrations. They also influence the non-stoichiometry of bulk UO_2, all of which are fundamental to understanding uranium self-diffusivity (see Robbe et al. [9]). However, it should be remarked that these results depend on the initial choice of the prior ranges for the atomistic-scale parameters. Note that although the sensitivity of creep rates to T_0 and H_{fpo_2}, as displayed in figure 3.1, is small compared to other parameters, they are the only parameters that are expected to vary between experiments as they define the experimental conditions. Hence, these two parameters are crucial to explain fine discrepancies between the experiments, and are to be included in the reduced model.

3.1.2 Neural network surrogate

Since many model evaluations are typically required for inference, the computational cost of the model must be taken into account. Therefore, the creep model is replaced with a NN surrogate

model using a subset of the most important parameters from figure 3.1. Included in these parameters are H_{fpO_2} and T_0, which describe the oxygen partial pressure, and are unique for each experiment that measures creep rates. Figure 3.2 shows a parity plot of the NN surrogate predictions and the model predictions for each experiment. The reported test errors represent the mean square error loss on the test data. Notice the overall excellent agreement between model predictions and surrogate predictions. During calibration, an average of 51 NN model evaluations per second was recorded representing a dramatic speed up on the full model, which takes $\sim$2 seconds to evaluate.

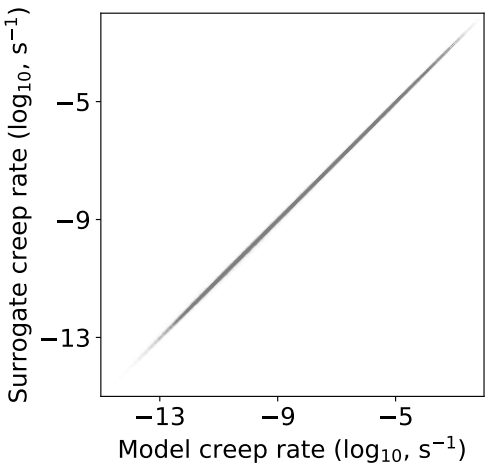

(a)

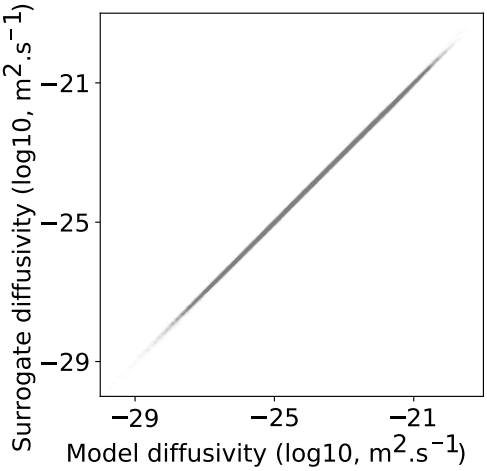

(b)

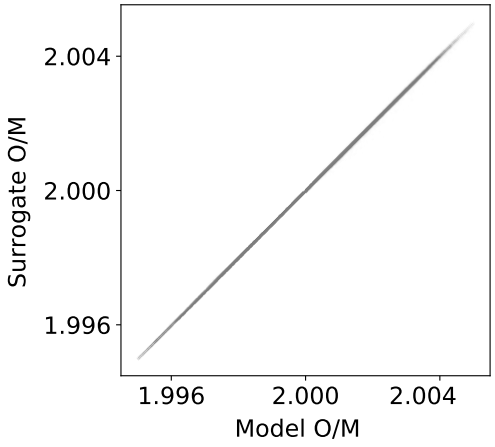

(c)

Figure 3.2: Comparison of the predicted outputs from the NN surrogate model and the actual model outputs. a) shows the comparison for the Armstrong [1] creep predictions, b) shows the uranium self-diffusivity [8], and c) shows the non-stoichiometry measurements (references within [9]).

3.1.3 Model calibration

The experimental conditions T_0 and H_{fpO_2}, describing the oxygen partial pressure conditions, are unique for each measurement group, and they are allowed to vary independently during calibration. This increases the number of parameters to infer from 14 to $12+2\times 31=74$ across the whole experimental set (for a given experiment there are 14 parameters). Together with the standard deviations σ_j of the residual uncertainty from Equation (2.2), this results in a total of $74+31=105$ parameters to infer.

The prior distributions are assumed to be uniform between the given lower and upper bounds, see table A2 in the Appendix. A standard normal prior is assumed for the log of the standard deviations of the measurement noise. Putting a prior on log σ_j ensures that values of σ_j are positive.

The MCMC algorithm outlined in 2.2.1 is run for 10^7 iterations using an adaptive proposal with an initial jump size of 0.8. In order to obtain good starting values for the chain, a few iterations with the deterministic optimization method L-BFGS are performed. The first $100,000$ states are discarded to avoid burn-in and the remaining states are thinned with a sub-sampling factor of 100 to reduce the auto-correlation of the samples.

Figure 3.3 shows the marginal posterior distributions for some select parameters, common across the experiments, where the minimum and maximum on the x-axis define the prior bounds. The orange line is the kernel density estimation, that is, a method for estimating the probability density of a dataset by averaging smooth curves (kernels) centered at each data point. H_{fpO_2} and T_0 are free to vary for different experiments (see figures A1, A2, A3, A4 in the Appendix), to allow for different experimental conditions. H_{VU}, H_{Oi} and S_{Oi} have a sufficiently low sensitivity (see figure 3.1) so the values from lower length scale simulations are contained within the respective probability distributions. H_{UO2} is found to be most likely 0.2 eV lower than the nominal lower length scale result, while H_h is shifted $\sim$0.2 eV higher than the lower length scale result. S_{UO2} is most probably 1.5 k_B lower than lower length scale prediction. The distribution for $H^m_{VU,GB}$ exhibits a maximum 0.4 eV smaller compared to the lower length scale result. The distribution peaks for H^{seg}_{VU} and H^{seg}_{VO} are 0.7 eV and 0.8 eV higher than the lower length scale results, reflecting the limited set of special grain boundaries used in the atomistic simulations. This is the largest source of discrepancy between the calibration results and the atomic-scale calculations. Finally, the diffusion prefactor $D_0^{VU,GB}$ is at least two orders of magnitude larger than expected. However, during the calibration process, the Coble creep prefactor (42 in Equation (2.1)) and the defect volume at grain boundary ($|\Omega_{V_{U,GB}}|$ in Equation (2.1)) are combined with the prefactor ($D_0^{VU,GB}$) and it is therefore difficult to distinguish which has the greatest influence. Inferred standard deviation of the Gaussian noise distributions of the likelihood function, which describes the experimental measurement scattering as well as the difference between modeling and experimental results are presented in the Appendix figure A3.

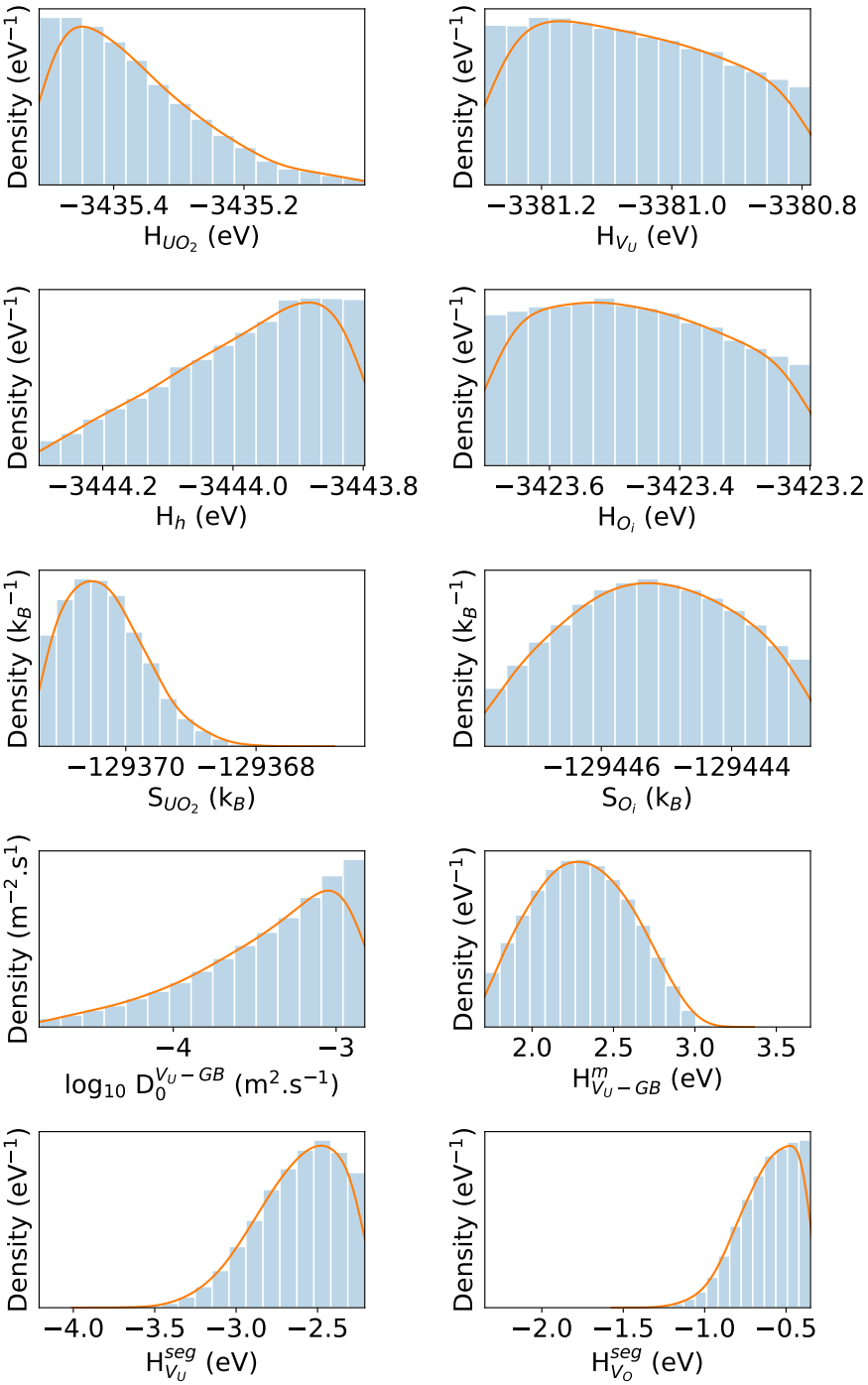

Figure 3.3: Posterior distributions for model parameters related to materials properties for creep, non-stoichiometry and self-diffusivity. For full parameter posterior distributions, see Appendix A1, A2, A3, A4. The histograms are shown in blue while the orange line is the kernel density estimate.

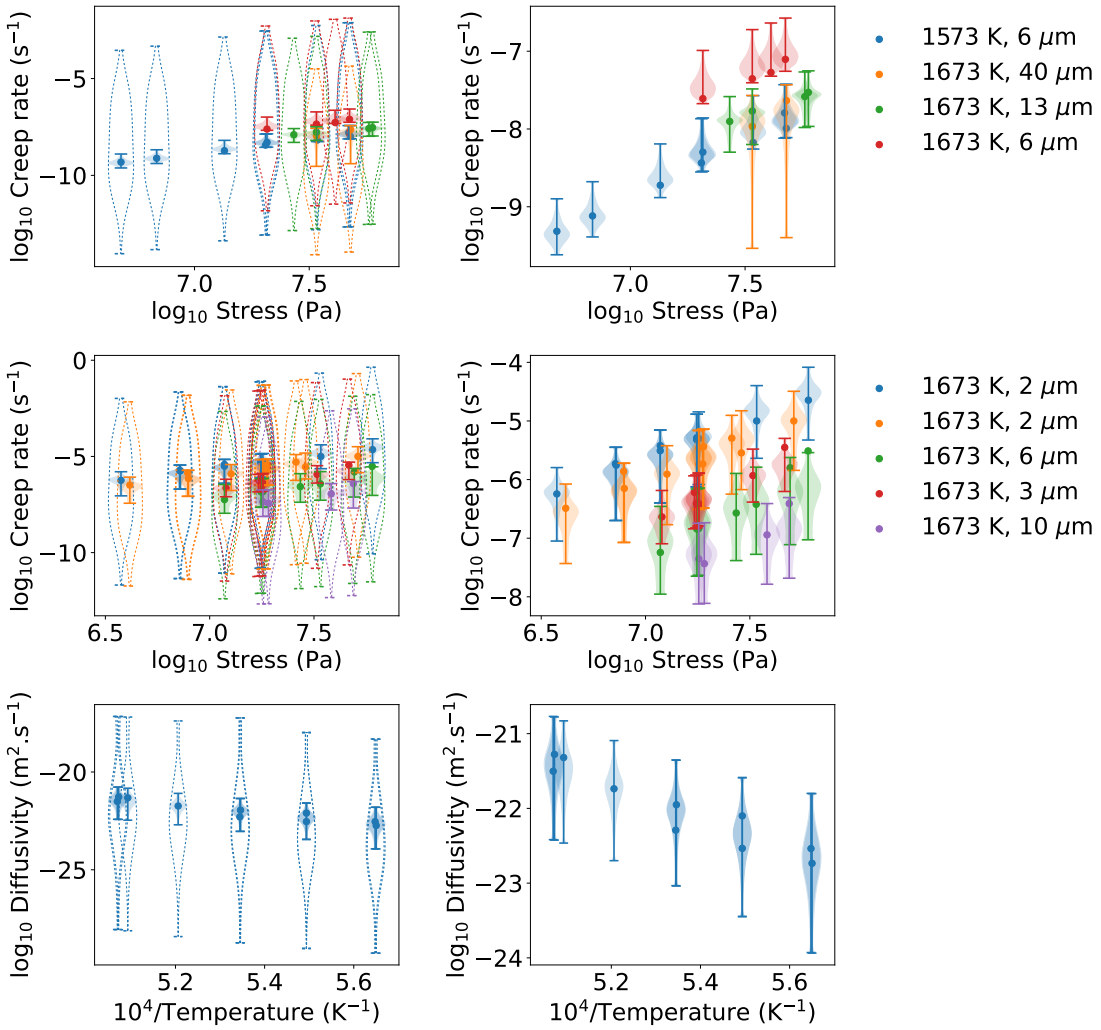

Figure 3.4: Pushforward posterior distributions for creep rate as a function of stress, and uranium self-diffusivity as a function of temperature. The dashed lines represent the prior and the transparent violins are the pushforward posteriors. Note that the right column is zoomed in on the pushforward posterior distributions where bounds are between 1^{st} and 99^{th} percentiles.

3.1.4 Pushforward posterior predictions

Once the models (bulk diffusivity, non-stoichiometry and creep rates) have been calibrated against experimental measurements using the NN surrogate models, predictions of creep (and self-diffusivity) with uncertainty are obtained by sampling the posterior parameter distributions and evaluating the model by pushing these joint distribution of parameters, preserving their dependencies, through the NN surrogate. This is known as the pushforward posterior, which is a multi-dimensional distribution, capturing the uncertainty for the creep rates and other properties based off the uncertainty of the posterior distributions.

Figure 3.4 shows an overview of prior and posterior distributions pushed forward to creep rate

measurements as a function of stress, and uranium bulk self-diffusion as a function of inverse temperature. For clarity, only 3 experimental datasets are shown, refer to the Appendix A5 for the complete set. It compares the pushforward prior and the pushforward posterior predictions, i.e., the distribution of model predictions evaluated at the posterior samples. The solid points refer to the experimental measurements, the solid transparent violin distribution (the width of each curve corresponds to the probability that the pushforward predictions, using the prior or posterior distributions, will evaluate at that creep rate or diffusivity value) represents the pushforward posterior, and the dashed violin distribution refers to the prior distribution. This highlights a large reduction in uncertainty from the prior to the calibrated posterior parameter distributions.

Using the most likely parameter set across that multidimensional space to explain the observed data values from the posterior distributions, the non-stoichiometry values for each UO_2 sample are predicted, and presented in figure 3.5. The solid points refer to the non-stoichiometry value for each experimental condition and the dashed lines are the resolution at which non-stoichiometry can be measured ($\pm$ 0.001). It can be seen that, even though the experimental measurements only include "nominally" stoichiometric data (experiments usually give a resolution of O/U = 2 $\pm$ 0.001 [49]) there is still significant variation that occurs in this range. This variation in non-stoichiometry, although small, has been previously shown to impact Coble creep rates in UO_2 [16].

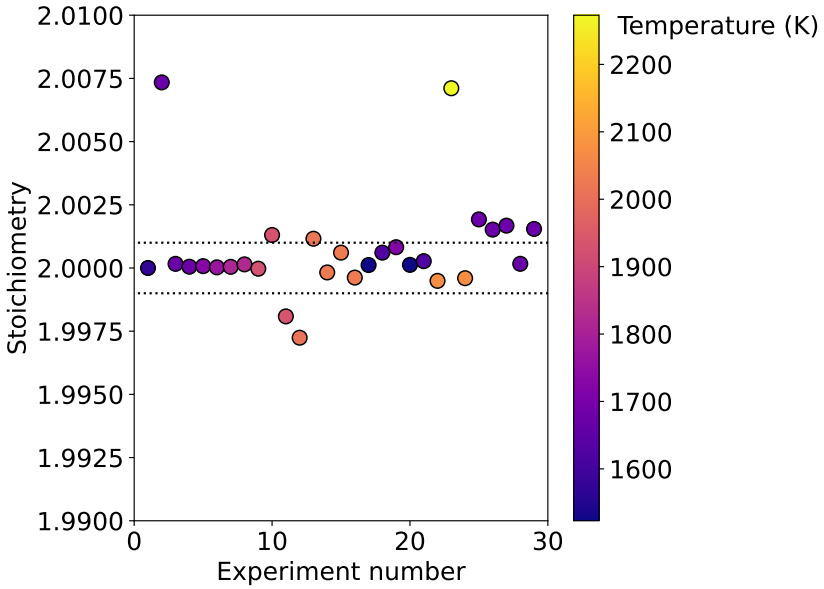

Figure 3.5: $UO_{2\pm x}$ as a function of each experimental condition. The colorbar gives the temperature that the measurement was carried out at. The dashed lines are an example of experimental "nominally" stoichiometric resolution at $\pm$0.001. The ordering for experiment number is the same ordering as in Table A1 in the Appendix.

Figure 3.6 shows the calibrated parity plot for the pushforward posteriors evaluated by the model against experimental measurements. The pink points are from the uncalibrated model (using atomic-scale parameters from the Σ9 grain boundary, see [26]). The blue points are the

most likely parameters values where the confidence intervals on the parameters are shown by blue violins. See A2 in the Appendix for parameter values. The top and bottom of the violin plots correspond to the 1^{st} and 99^{th} percentiles. The Posterior predictive distributions of creep rate as a function of stress for two experimental studies [1, 7] is shown in A6, these included the uncertainty due to model parameters and the residual uncertainty.

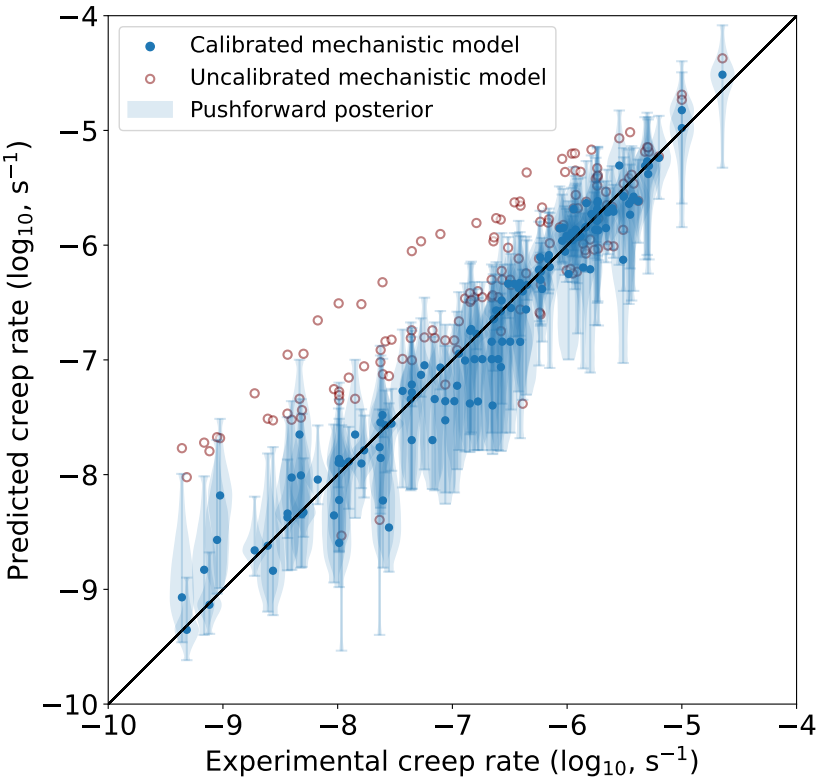

Figure 3.6: Parity plot of experimental creep rates against model predictions. The open points represent the uncalibrated model (using Σ9 grain boundary parameters from [26]) and the violin densities are the calibrated model with uncertainties. The solid blue points are the most likely parameters values for the calibrated model. Note that these violin plots display 98 percentiles of the distributions. Data below the 1^{st} percentile and above the 99^{th} percentile are filtered out in order to make the plots more readable, and to avoid displaying unnecessary long tails.

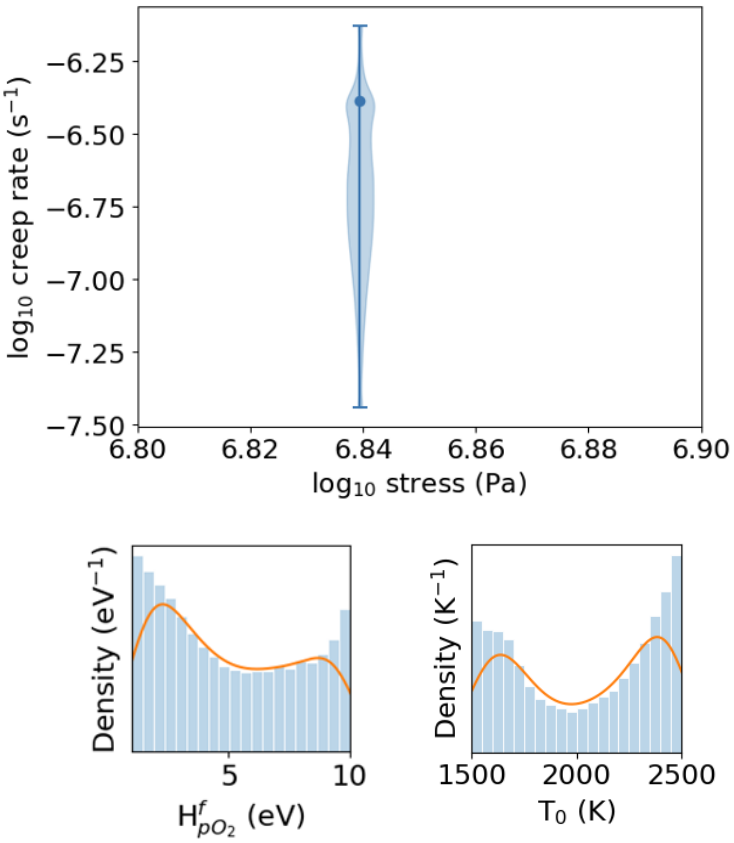

Figure 3.7: Pushforward posterior and corresponding H_{fpO_2} and T_0 posterior distributions for experimental creep measurement given by [5].

3.2 Data transfer to Idaho National Laboratory

From our previous work [11], an atomistic creep model was developed (included in the Bayesian UQ framework). Using this model, UO_2 creep rates, in the diffusional regime, were generated at various O partial pressure conditions, pO_2, for different stress, σ, grain size, G, and temperature, T as a lookup table. This was passed on to our collaborators at Idaho National Laboratory (INL), to fit a surrogate model, capturing the data, and to be implemented, along with other creep mechanisms from the refit MATPRO correlation by Sweet et al. [50], into BISON and tested for different assessment cases.

Using the most probable parameter values obtained from the Bayesian calibration in Section 3.1, the atomistic diffusional creep model was refined. In addition, we incorporated an irradiation creep model developed at lower length scales, based on atomistic and cluster dynamics simulations using the LANL Centipede code [26] updated with the most probable values from the UQ results. This enhancement enables us to extend the model's applicability to lower temperatures and account for the effects of fission rate.

3.3 Full–field simulations of plastic deformation and creep

In practice, creep behavior is highly complex and often cannot be fully captured by the simplified analytical models discussed earlier. Creep deformation in UO_2 presents particular challenges due to its sensitivity to local defect concentrations, stress states, and microstructural characteristics. Advanced material models are clearly needed, that are sensitive to microstructural features, capable of capturing local variations, and that incorporate both kinetic and kinematic effects, particularly for doped UO_2, where experimental data is limited. In this section, we introduce a crystal plasticity-based framework designed to predict the creep response of UO_2 and large grained (doped) UO_2, explicitly considering microstructural features. The model is informed by atomic-scale simulations and literature data, including mechanisms such as pipe diffusion. Full-field simulations of three-dimensional polycrystalline UO_2 and large grain (doped) UO_2 are conducted, with the contributions of dislocation climb and glide included in the resulting creep response. For doped UO_2 at conditions relevant to reactor operation, dislocation creep is expected to make a more significant contribution to creep that grain boundary diffusional creep, primarily due to the suppression in diffusional creep as a function of grain size.

3.3.1 Applied strain rate simulations of undoped and doped UO_2

Figure 3.8a, shows stress-strain curve predictions for UO_2, with varying grain size. This shows a decrease in the the steady state stress (yield point) with increasing grain size. This change can be attributed to the Hall-Petch effect which increases hardness for smaller grain sizes. The Hall–Petch effect describes how reducing the grain size of a polycrystalline material increases its strength and hardness. In essence, grain boundaries serve as barriers to dislocation motion, so having more of these boundaries per unit volume (i.e., smaller grains) makes it harder for dislocations to move through the material. As a result, smaller grains increase the stress required to initiate and sustain plastic deformation, increasing the materials hardness and yield strength. This compares well with the experiments carried out by Dugay et al. [10] (see figure 3.8b) where a reduction in yield stress is observed for the Cr-doped UO_2 which corresponds to a larger grain size.

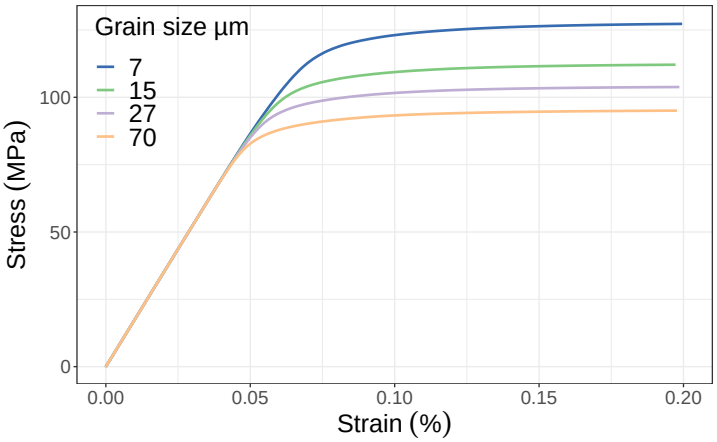

(a)

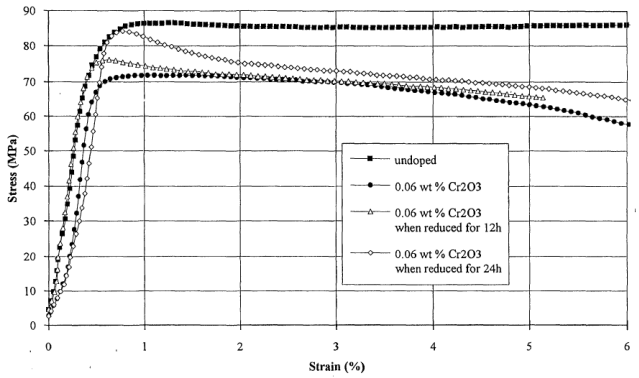

(b)

Figure 3.8: (a) LApx simulation results for the same conditions showing the impact of different grain sizes. (b) Plot from the experimental paper of Dugay et al. [10] of effect of reduction on the deformation of the batch doped with 0.06 wt% Cr_2O_3 under a constant applied strain rate of 20 μm/min at 1500 °C.

However, in the work of Dugay et al. [10] a saturation effect for larger grain size Cr doped UO_2 is observed, see figure 3.9b. Therefore, to investigate a possible cause, we have included the solute back stress for diffferent amounts of Cr %. Solute back stress refers to the internal stress generated by interactions between dislocations and solute atoms in the material. Over time, the build-up of solute atoms around the dislocation line produces an opposing force (or "back stress") that resists further dislocation motion. This effectively could raise the flow stress or yield strength of the material, as an increased applied stress is required to overcome the dislocation–solute interaction. As a result, materials with greater solute concentrations or more effective solute–dislocation binding can exhibit higher strength through this solute back stress mechanism. For the solute back stress model, not all the parameters are known for UO_2 so best estimates were used focusing on the impact rather than provide high fidelity predictions of values. This will be investigated further in future work. The simulation results, which consider

various grain sizes and corresponding Cr solute concentrations, are presented in Figure 3.9a, where we compare the initial softening of the Cr-doped sample (at 1773K) and a saturation effect for larger grain sizes.

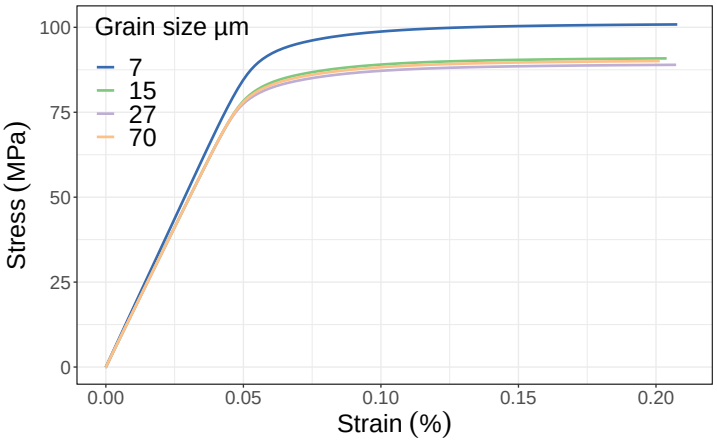

(a)

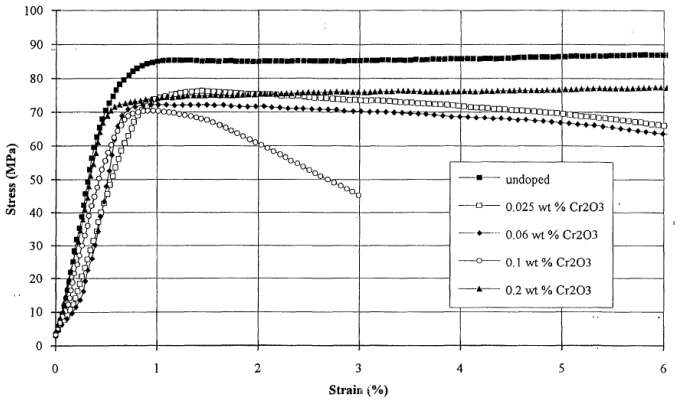

(b)

Figure 3.9: (a)LApx simulation results for different grain sizes with the impact of different levels of Cr impacting solute pinning. (b) Plot from the experimental paper of Dugay et al. [10] for different doped UO_2 samples containing different levels wt% Cr under an applied strain rate of 20 μm/min at 1500 °C. 0.025 wt% Cr_2O_3, 0.06 wt% Cr_2O_3, 0.1 wt% Cr_2O_3 and 0.2 wt% Cr_2O_3 correspond to grain sizes of 15, 27, 45 and 70 microns, respectively.

3.3.2 Applied stress simulations of undoped UO_2

Figure 3.10 presents the strain rate as a function of applied stress, comparing experimental data, LApx (dislocation model) simulation results, and the analytical diffusional model developed in our previous milestone [11]. The analytical diffusional mechanistic model, accurately describes the experimental behavior at lower stress levels but significantly underestimates the plastic de-

formation at higher stresses due to the omission of dislocation mechanisms. In contrast, the LApx simulation results, which incorporate dislocation climb and glide (diffusion is not included in these LApx simulation runs), exhibit good agreement with the experimental data in the high-stress regime.

- At low stresses (below 90 MPa), the creep response is dominated by diffusional processes, with grain boundary dislocation nucleation, as described by Dillon et al. [51], having a rate limiting effect below 20 MPa.
- Around intermediate stress levels ($\sim$90 MPa), dislocation climb begins to contribute meaningfully to the total creep rate and eventually becomes the dominant mechanism.
- At the highest stress levels (above 120 MPa), the glide contribution takes over as the primary driver of creep.

By including different modeling approaches (informed by atomic scale simulations), we achieve a description that captures the transition between the various creep mechanisms active in undoped UO_2. Given the amount of experimental data available for undoped UO_2 (compared to doped UO_2), it serves as a valuable benchmark for validating the proposed models. Moreover, this model shows that glide might have an important role (if those stresses are reached by the fuel pellet in reactor), which is currently not implemented in the MATPRO empirical model used in BISON. In the following section, we extend this model to investigate the influence of large grain (doped) UO_2.

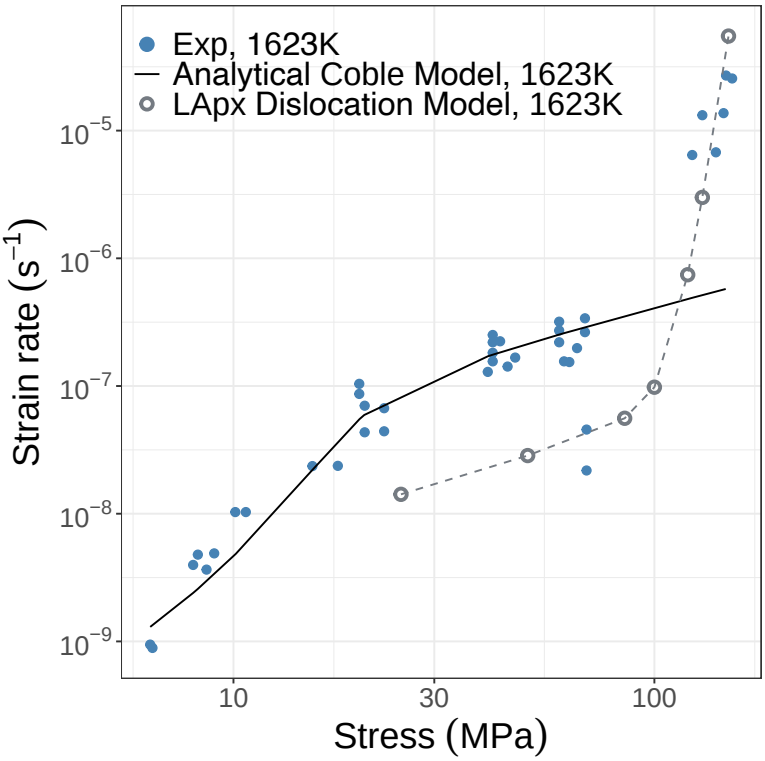

Figure 3.10: UO_2 creep rates as a function of stress. LApx points are shown as open circles (with a dashed line shown for visualization purposes) and the diffusional mechanistic model [11] as a line. Experimental points are shown in blue.

3.3.3 Applied stress simulations of doped UO_2

Figure 3.11 shows our simulation results alongside experimental data from Dugay et al. [10] and other sources [2–4,6,7,17–25] (from this dataset creep rates matching the temperature, grain size and stress of Dugay et al. were used). Notably, the undoped UO_2 data reported by Dugay (shown by blue points) exhibit distinct behavior compared to other experimental datasets collected under similar conditions (shown in black). Despite this variation, the LApx predictions for undoped UO_2 (represented by open circles) align well with the experimental measurements shown by the black points for undoped UO_2. In this stress regime, where there is data to compare, dislocation climb is the dominant mechanism, as indicated in figure 3.10, and therefore, the Hall–Petch effect is not expected to play a role. In this model Hall-Petch only impacts the glide mechanism, as evident in the stress-strain curves shown in figure 3.8a (which are glide dominated) and the strain rates shown in figure 3.12. To extend the model to doped UO_2 in the climb regime, we account for microstructural changes by increasing the grain size of the structure and also slightly raising the dislocation density by a factor of two. We believe the adjustment is a physically reasonable assumption: the substitution of chromium into the UO_2 lattice likely introduces local lattice strains due to the mismatch in ionic size and valence between chromium and uranium ions, potentially creating favorable sites for dislocation nucleation. Additionally, the modified defect

chemistry may reduce the energy barriers associated with dislocation formation and motion.

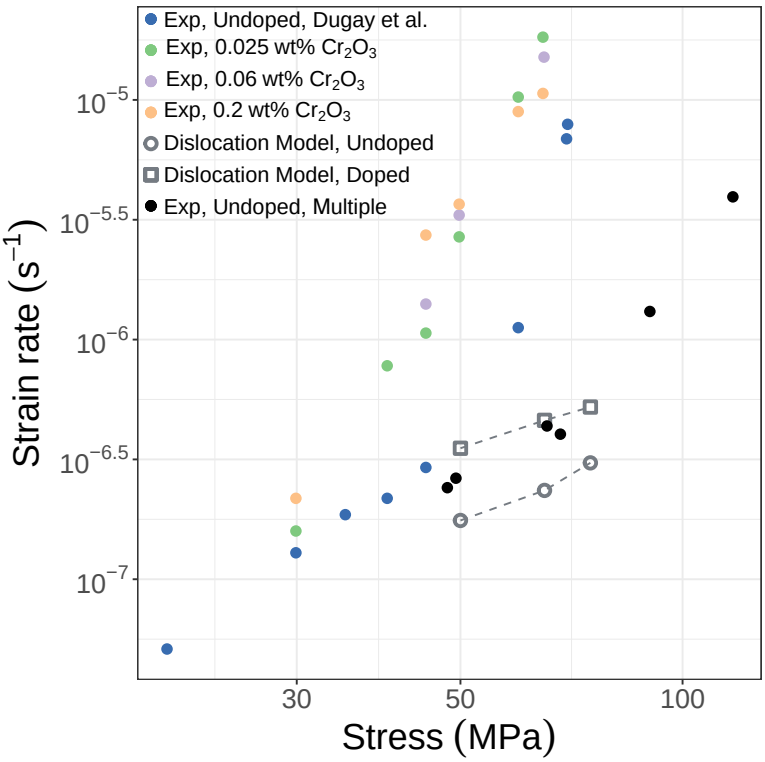

Figure 3.11: Creep rates as a function of stress at 1773 K. LApx points for undoped UO_2 are shown as open circles and for doped UO_2 as open squares. Doped experimental data and undoped (blue points) is from Dugay et al. [10]. Undoped experimental data (black points) is from other sources [2–4, 6, 7, 17–25].

Figure 3.12 shows the LApx predictions of strain rates for different grain sizes. At a stress of 50 MPa, no grain size dependence is observed for the dislcoation model, as indicated by the overlapping data points. This is expected, given that at this stress and a temperature of 1623 K, LApx predicts climb as the dominant deformation mechanism (noting that diffusion effects are excluded from these simulations). However, there is a suppression of the Coble diffusional mechanism, seen from the diffusional mechanistic model [16]. As the stress increases and dislocation glide begins to influence, and eventually dominate the deformation behavior, the impact of the Hall-Petch effect becomes apparent. Consequently, enhanced creep rates are observed in large-grained (doped) UO_2. The competition between enhanced glide and suppressed Coble will be analyzed in BISON for realistic in-reactor conditions for future work, discussed in more detail in section 4.2.

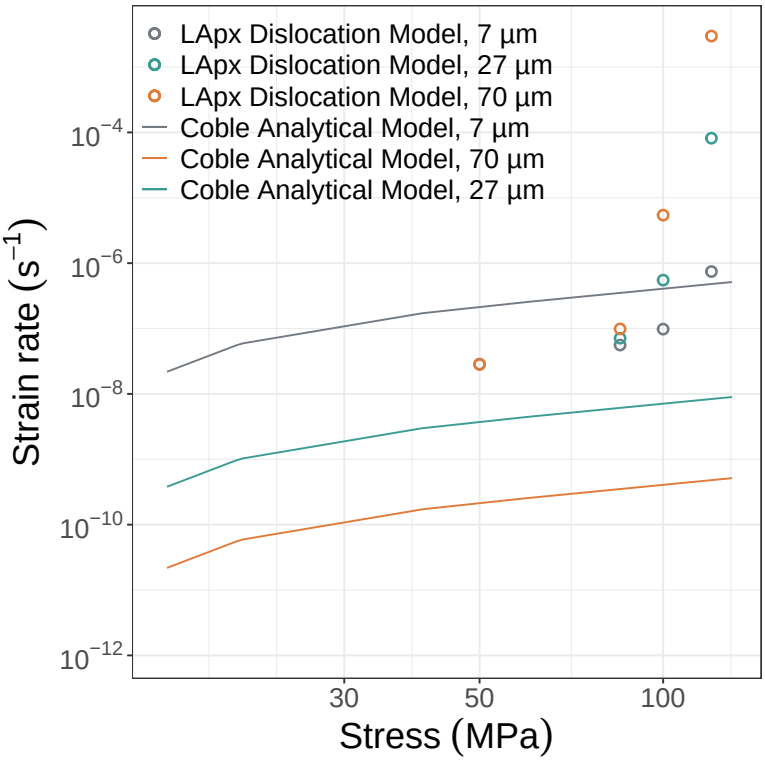

Figure 3.12: LApx predicted creep rates as a function of stress for three different grain sizes at a temperature of 1623 K. The mechanistic diffusional model is also shown (Coble).

4 Discussion and Future Work

4.1 Uncertainty quantification

4.1.1 Importance of mechanistic models

Mechanistic models informed by lower length scale modeling provide benefits over traditional empirical models only fit to experimental data. For instance, they need fewer data points for fitting, have common parameters across different materials models, and can be extrapolated (with large uncertainty in a data-scarce region) provided that they include the correct underlying physics. By parameterizing fuel performance codes (e.g., BISON) using mechanistic models with data from lower length scales [52, 53], it is possible to describe chemical and microstructural evolution rather than having empirical models only fit to burnup and temperature or semi-empirical models that incorporate separate effects data but without detailed knowledge of the underlying processes. This study gives a working example of combining uncertainty quantification with mechanistic modeling informed by the lower length scale data to show it has an important role to play in the ambitious challenge of AFQ.

4.1.2 Application of UQ to diffusional creep mechanistic model

A Bayesian calibration framework is used to analyze the atomic-scale-informed creep model along with experimental measurements in [16]. Similar to Robbe et al. [9], additional constraints are applied to the underlying model parameters by calibrating the uranium bulk self-diffusion and non-stoichiometry predictions against available experimental data. Using nominal parameters (not calibrated) of the creep model from [26], a good description of the experimental creep measurements is obtained. Most importantly, the model accounts for both bulk (Nabarro-Herring) and grain boundary (Coble) diffusional creep showing that Coble was the only mechanism capable of explaining the observed creep rates in the diffusional regime: Nabarro-Herring, based on bulk diffusivity, was many orders of magnitude too low. Even accounting for conservative uncertainties on the underlying parameters this qualitative conclusion is valid. Furthermore, separate effects tests on single crystal bulk self-diffusivity validate the atomic-scale parameters used to conclude that diffusivity influencing Nabarro-Herring is too low to explain the creep measurements.

Despite the work of Galvin et al. [16] demonstrating that Coble creep is necessary to get modeling results in the correct order of magnitude compared to the experiment, there were some experimental data not predicted correctly by the model and that indicate grain size dependencies with exponents not equal to 3 (an essential criterion for Coble creep as shown in Equation (2.1)). Galvin et al. speculated that small deviations in non-stoichiometry for samples with different grain sizes, arising either from different fabrication conditions or measurement conditions, could

explain this discrepancy. They showed that deviations of just ± 0.01 resulted in order of magnitude changes in the creep rate if experiments have slightly different conditions - this is sufficient to interfere with the grain size dependence and can explain the scatter shown in figure 3.6 for the uncalibrated model. The objective of this work is to use Bayesian techniques to determine to what extent the scatter in figure 3.6 is due to experimental instrumentation uncertainty, lack of information regarding experimental conditions that can be inferred in this work, and/or inaccuracies in the underlying atomic-scale parameters, which can be corrected through inference resulting in posterior distributions of the parameter sets.

Using a Bayesian framework, a systematic calibration of this mechanistic UO_2 creep model is conducted in a way that incorporates uncertainty and prior knowledge, leading to more meaningful predictions and more confident conclusions about the underlying processes being studied. Conservative bounds were set on the prior uncertainty, which means propagated uncertainties on the predicted creep rates (using just the prior) would be too large to be accepted during the qualification process (see the dashed violins in figure 3.4). Despite this, the parameters informed by lower length scale simulations were vital to constrain the diffusional creep model to have the correct mechanism (i.e. Coble and dominated by uranium vacancies [16]). This is extremely important when carrying out the inference process. If, as an example, the wrong mechanism was used for the calibration (i.e. Nabarro-Herring) a seemingly 'sensible' answer would have been obtained for the creep results but for the wrong reasons. The model extrapolation would not be correct (as Coble and Nabarro-Herring have different grain size dependencies), the experimental measurements could not be re-analyzed using the non-stoichiometry conditions (as the oxygen partial pressure predictions would be wrong), and we would lose the ability to use the common parameters to span other experiments and validate using separate effects testing, see section 4.1.5.

4.1.3 Importance of controlled experimental conditions

A sensitivity analyses was conducted to rank the impact of the underlying parameters for the diffusional (Coble) creep model on the experimental measurements, and is shown in figure 3.1. Although a different surrogate is used in this work, the most sensitive parameters for the uranium bulk self-diffusion agree with that of Robbe et al. [9]. This not only allowed the parameter set to be reduced for training of the NN surrogate, but can enable common parameters that impact properties important for qualification to be identified. For example, parameters that impact cladding stress state through pellet-cladding-mechanical interactions during a LOCA scenario rather than UO_2 creep rates more generally. This will prioritize experiments to probe relevant parameters for qualification, not just for making the best overall creep model.

Controlled p_{O_2} experiments (similar to those by Garcia et al. [54]) would be of value as it would allow targeting reducing uncertainties in important parameters. The $H_{fp_{O_2}}$ and T_0 parameters, which are needed in this work to predict p_{O_2} because accurate p_{O_2} (and, therefore non-stoichiometry) values are not provided by the experiments, could be dropped from the model and replaced with p_{O_2} values directly. Then the calibration would drop a layer of complexity and focus more so on the defect enthalpy and entropy parameters also reducing their uncertainties. Although we infer $H_{fp_{O_2}}$ and T_0 for each study, showing that minor variations in non-stoichiometry can explain the differences in creep measurements, it is possible that other

systematic errors are being included in those variations. These errors could be addressed with experiments that provide tighter stoichiometry control.

4.1.4 Surrogate models

NN surrogates were trained on the mechanistic model data randomly sampling the most important parameters identified using a sensitivity analysis, see figure 3.2. The surrogate models are necessary, as they allow rapid evaluations during the MCMC sampling process. In this work, for the calibration to converge, $\sim 10^7$ iterations are needed, and, therefore, it becomes apparent that without using a surrogate this quickly starts to become unfeasible. For the full model, each MCMC iteration requires about 2 seconds for a single evaluation. Over 10^7 MCMC iterations, this leads to a total computational cost of 2×10^7 seconds ≈ 231 days. For the surrogate model, we can evaluate approximately 51 samples per second. Thus, the total cost for performing 10^7 iterations becomes 1.96×10^5 seconds ≈ 48 hours. Hence, the surrogate approach is approximately 100 times cheaper in terms of computational cost compared to the full model. Moreover, this issue becomes compounded if additional models are to be included (e.g. Xe diffusivity under irradiation which relies on cluster dynamics simulations [9, 55]) which would increase the calibration convergence time.

Surrogate models are also important for propagation to the engineering-scale (see Matthews et al. [56]). This is a feasible way to provide lower-length scale informed correlations to target data science applications or other large scale computational models, e.g., full reactor simulations. While we employed simple adaptive MCMC for Bayesian inference, more advanced sampling algorithms could be used to further accelerate convergence. Methods such as the Differential Evolution Adaptive Metropolis (DREAM) [57], Hamiltonian Monte Carlo (HMC) [58], and Sequential Monte Carlo (SMC) [59] are designed to improve sampling in high-dimensional or multi-modal posterior landscapes. These techniques leverage parallelism, gradient information (in the case of HMC), or population-based strategies (as with DREAM) to accelerate convergence and improve exploration of complex parameter spaces. However, they introduce additional algorithmic parameters and tuning requirements, which can complicate their implementation.

4.1.5 Parameters that influence other aspects of fuel performance

The phenomena investigated in this work are governed by common underlying parameters. Applying the same framework to calibrate parameters common to different types of experiment would i) allow to further reduce uncertainties, and, ii) provide lower-length scale parameters with associated uncertainties to parameterize mechanistic engineering-scale models. For instance, uranium vacancy behavior is not only fundamental to UO_2 creep, self-diffusion in the bulk and grain boundary, but also contributes to inter-granular bubble swelling and Xe diffusion under irradiation conditions [9,55]. As an example, this approach could also make it possible to conduct creep experiments to validate fission gas models where experiments are more difficult and costly to conduct, provided the underlying mechanisms play a significant role. Therefore, by combining mechanistic models with the same underlying parameters, that influence a variety of fuel behavior, and passing these up to the engineering scale (e.g. BISON), separate effects

tests can be conducted to reduce the overall uncertainty.

4.1.6 Re-analyzing the experimental creep rates

Figure 3.4 shows the pushforward posterior distributions, i.e., the model predictions taking into account the uncertainty due to model parameters alone. Notice that the pushforward posterior distributions shown by the transparent violins in figure 3.4 encapsulate all the experimental measurements (solid points), and drastically reduce the prior uncertainty (dashed violins). This means (assuming the mechanistic model is correct) the experiments can be explained by the model, even though all experimental points are from different studies, with various environment conditions, temperatures, grain sizes, and stresses. This is therefore a powerful tool as it allows us to re-analyze the experimental data in a new context.

Examining the posterior distributions in 3.7, a bimodal shape is observed for H_{fpO_2} and T_0 for the creep measurement given in [5], see figure 3.7. This is a large grain (55 μm) experimental measurement supposedly in the diffusional regime. This is shown in [5] by a line indicating this point lies in the diffusional regime (see Figure 20 in [5]). However, this bimodal distribution suggests that there are two solutions that satisfy H_{fpO_2} and T_0 after calibration. This means that there are two oxygen partial pressure solutions that could explain this measurement. By re-analyzing the experimental measurement it can be assumed that this is in a regime where another mechanism not described by the model (e.g. climb) is active.

Another example pertains to the Armstrong creep measurements [1]. For this data set, the 40 μm grain size does not behave as expected. In their study it is seen that when the creep rate is plotted against stress and the stress exponent is $\sim$1 (i.e. the diffusional creep regime) the 40 μm grain size shows similar creep rates for a grain size of $\sim$13 μm. To obey Coble creep (Equation (2.1)) the creep rates should be suppressed following an inverse cubed relationship with grain size. This is discussed in [1] and [5], with explanations being suspected grain boundary sliding. As the data has a stress exponent of 1 it should not have a dislocation limited climb or glide contributions. Another possibility would be the presence of Harper-Dorn creep [21], but we do not believe that to be the case due to the slow mobility of uranium vacancies in the bulk lattice [16]. After calibration it is shown that the 40 μm grain size Armstrong creep rates [1] have larger uncertainty compared to the other data (see figure 3.4). Examining the slight deviations in non-stoichiometry of the UO_2 sample accounted for in calibration indicated that these points would have to be more hyper-stoichiometric than the other measurements, however due to the large uncertainty it is also plausible that the data is in another creep regime. The UO_2 non-stoichiometery values, a consequence of the chemical environment or conditions that these creep measurements were conducted under, are inferred.

The predicted non-stoichiometry for each experimental condition using the most probable values after calibration in the model is shown in figure 3.5. What this shows is even slight changes in stoichiometry can impact creep rates dramatically. The dashed horizontal lines in figure 3.5 represent good experimental resolution, and within these bounds (from an experimental point of view) UO_2 can be classified as 'nominally' stoichiometric. It is observed that most of the data lies within these bounds but still exhibit some variations in non-stoichiometry. Moreover, a few data points are slightly hypo-stoichiometric. These are at high temperatures ($>$1900 K), where, according to the UO_2 phase diagram [60], UO_2 can be slightly hypo-stoichimetric. The singular

creep measurement of [5] is shown to be slightly hypo-stoichiometric, but exhibits a bimodal posterior distribution. So although it can be described by non-stoichiometry, it is likely that it is in the climb creep regime.

4.1.7 Industry perspective

Industry is the ultimate user of the AFQ methodology. For industrial purposes, hardware (e.g., fuel pellets) and software (fuel performance simulation tools) are combined in the product (licensed fuel). Fuel is designed to maximize the amount of power that can be extracted for a given volume and residence time, and operational behavior for each pin has to be verified to guarantee the safety of the reactor. This is done through the use of fuel performance codes, relying on models. To be conservative, uncertainties have to be taken into account, usually in a best estimate plus uncertainty (BEPU) approach. It is straightforward from there that larger uncertainties result in less optimized operating conditions, and therefore in a direct financial loss for the plant operator.

The industry has been moving toward a Bayesian inference uncertainty quantification approach instead of BEPU. This is a shift in paradigm; uncertainties have been split in three main categories: a) the material specifications, b) the reactor operating parameters and c) the material properties, and each one has a probabilistic distribution, whereas in BEPU, (a) and (b) parameters are considered 'true' model parameters and only the (c) category is considered. This new method allows for simultaneous calibration and uncertainty determination, and the hope is that by not treating models individually, the overall uncertainty decreases, reducing the required safety margins.

When a new material is developed, material property models have to be derived or calibrated, and the relative lack of data as compared to UO_2 and Zr alloys forces larger uncertainty, reducing dramatically the benefits of the new material. This is exacerbated when the available data comes from unconventional sources, such as separated effect experiments or lower length scale modeling, as is the concept behind AFQ. While BEPU has problems with both the determination of the best estimate in prototypical conditions and the lack of knowledge of the uncertainty, a Bayesian calibration approach at the lower length scale or engineering-scale can permit the determination and reduction of uncertainties, and is as such an integral part of AFQ.

4.2 Dislocation based mechanisms for creep in UO_2 and doped UO_2

LApx is a simulation tool based on models like elastic, plastic, and visco-plastic behavior. It is designed to help explore complex links between processing, structure, and properties, phenomena that are difficult to capture with simple analytical equations (even if informed from lower length scale simulations). To make sure the simulations reflect how materials really behave, the model relies on many parameters that need to be updated with lower length scale information or carefully calibrated to experiment.

Figure 3.8a shows that for large-grained UO_2, the Hall-Petch effect results in a reduction of stress in the stress-strain curves. This is because the Hall-Petch relationship, which predicts increased strength with decreasing grain size, weakens as grain size increases. In large grains,

dislocations encounter fewer grain boundaries, which are primary obstacles to their motion, however, other obstacles must be considered when burnup is accounted (e.g. bubbles and precipitates). This results in dislocation glide, the dominant plastic deformation mechanism at high stresses for these simulations, becoming easier, requiring less applied stress to sustain deformation. This leads to a softer mechanical response for high applied stresses. As Cr-doped UO_2 has larger grains this could be part of the reason why a softer mechanical response is observed for doped UO_2, as shown by the experimental measurements of Dugay et al. [10] (see figure 3.8b). However, this seems to be temperature dependent. A recent LANL report by Butler et al. [61] for the AFC program has shown that Cr-doped UO_2 can actually produce higher stresses compared to undoped UO_2. Their measurements were taken at lower temperatures (ranging from 1173 K – 1623 K) compared to the work of Dugay et al. [10] and it is hypothesized that strong pinning of dislocations could be the cause at lower temperatures. Furthermore, although there is an initial softening of the material for larger grains, Dugay et al. [10] observed a saturation effect where no matter the grain size, the results where similar for large grain Cr-doped UO_2 as shown in figure 3.9b. To explore the impact, we have included solute pinning effects in the simulations (see figure 3.9a). We first calibrate the value of the Hall-Petch parameter to yield similar results to undoped UO_2, and then run simulations under the same conditions as Dugay et al. [10] for the different samples of Cr-doped UO_2. Despite incomplete knowledge of all input parameters for solute pinning behavior, the simulation results from this parametric study indicate that solute pinning plays a significant role in the onset of saturation behavior.

LApx simulations that incorporate atomic-scale information are able to capture this behavior accurately, even when not all material parameters are precisely known. Future work will be to explore the parameters that impact solute pinning behavior and the temperature dependence. Collaborating closely with the LANL experimental team on the AFC program to carry out doped UO_2 measurements will yield invaluable data for calibrating our models and identifying the underlying processes. For instance, experimental tensile and creep tests comparing undoped large-grain UO_2 with similarly grained doped UO_2 would be particularly informative. Conversely, the models developed within the NEAMS program can also support the interpretation of the experimental results.

Applied stress simulations have also been conducted using the LApx polycrystalline code. For these simulations a good agreement with UO_2 experimental measurements (at high stresses) is predicted, see figure 3.10. Our previous diffusional mechanistic models [11,16] are not able to capture the dislocation and glide mechanisms, which are dominant at higher stresses. At lower stresses, the diffusional creep regime dominates, as shown previously [16]. As stress increases, dislocation climb becomes increasingly significant, leading to a regime where both climb and diffusion contribute. With further increase, the behavior transitions to climb-dominant, followed by a combined climb and glide regime. At high stresses (above 100 MPa), dislocation glide becomes the dominant mechanism. Specific regions of a fuel pellet can reach the temperatures and stresses needed to initiate glide before pellet cracking. This is important as larger grain doped UO_2 creep rates can be enhanced in the glide regime due to the Hall-Petch effect (see figures 3.8a and 3.12). These enhanced creep rates could produce better pellet cladding mechanical interactions. Implementing this behavior into BISON is important for future work as it will enable predictions of how pellet cladding interactions impact cladding rupture (under LOCA conditions) for doped UO_2. Furthermore, it will allow the competition, in large grain

doped UO_2, between hardening due to suppressed Coble creep at low temperatures and stresses against softening due to enhanced glide at high stresses and temperatures to be examined or realistic in-reactor conditions. Other future work will include taking advantage of the rate theory capabilities in LApx to account for irradiation damage due to burnup.

The undoped LApx creep model has been extended to predict creep rates for Cr-doped UO_2 and compare to the experimental measurements of Dugay et al. [10], shown in figure 3.11. The first point to highlight is the discrepancy among experimental measurements for undoped UO_2. Data from Dugay et al. [10] show a sharp increase in creep rates below 75 MPa, potentially indicating the onset of glide. However, this trend is not observed in other experimental datasets [2–4, 6, 7, 17–25] (from this dataset creep rates matching the temperature, grain size and stress of Dugay et al. were used). Our model predictions align more closely with the measurements not conducted by Dugay et al., suggesting that glide does not become dominant until higher stresses (above 100MPa). Additional experiments under the AFC program would help clarify the reasons behind these discrepancies. Moreover, comparisons with doped UO_2 experiments at similar stress levels (around 50 MPa) suggest that we are firmly within the climb regime for LApx predictions (these LApx simulation runs do not include contributions from the diffusional regime), where both dislocation climb and diffusional creep contribute to the overall creep behavior. This means that the Hall-Petch effect will not contribute here as it did in the tensile test simulations. For these simulations we have increased the dislocation density to account for the addition of Cr. This shows an increase in creep rates compared to undoped UO_2 suggesting that it has a contribution. However, we know that diffusion of uranium vacancies in the bulk and at dislocations have a role to play. Therefore, future work using atomistic simulations investigating the impact of Cr on the diffusion of uranium vacancies at dislocations will be conducted.

This model incorporates a wide range of input parameters, from lower-scale simulations, experimental observations, and interpolated data. These inputs come from many sources and vary significantly in terms of reliability and accuracy, some are well-established, while others carry considerable uncertainty. Due to the model's inherent complexity, it is important to understand which parameters exert the greatest influence on its predictions. To guide future efforts, a sensitivity analysis (as done for the analytical diffusional mechanistic model) will be carried out to prioritize the most important inputs. Going one step further, applying the model to the Bayesian uncertainty framework (shown for the diffusional mechanistic model in this report) will provide crucial understanding of how uncertainties in input parameters translate to uncertainties in creep rates. Furthermore, by incorporating new experimental measurements into the UQ framework, the overall model uncertainty can be reduced. An additional benefit of this would be to reduce uncertainties in other mechanistic models being informed by the same underlying atomic scale parameters, such as fission gas release models for doped UO_2.

5 Conclusions

In this study, we built upon our previous work [11, 15, 16] to achieve three key objectives aimed at advancing the modeling of creep mechanisms in UO_2 and and developing a creep model for Cr-doped UO_2.

- First, we applied a Bayesian uncertainty quantification (UQ) framework to evaluate the uncertainty in our lower length scale UO_2 diffusional creep model, providing a comprehensive assessment of model reliability and parameter variability.
- Second, we refined the mechanistic diffusional creep model for UO_2 by incorporating the most probable parameter values obtained from Bayesian calibration and adding an irradiation-driven component to account for fission rate effects. This refinement prepares the model for eventual integration into BISON, supported by a dataset we generated for INL to use in training a reduced-order model surrogate.
- Lastly, we explored the roles of dislocation climb and glide mechanisms within a lower length scale-informed viscoplastic framework for both UO_2 and Cr-doped UO_2. For this, we conducted tensile (stress-strain) simulations for doped UO_2 to identify the mechanisms responsible for softening for larger grain sizes, and compared these results to experimental measurements. Additionally, we performed simulations to predict creep rates for undoped UO_2 and extended the model to investigate the origins of the enhanced creep rates observed in doped UO_2.

These advancements represent a significant step toward the development of mechanism-based creep models for eventual implementation into BISON.

Acknowledgments

Funding for this work was provided by the US Department of Energy, Office of Nuclear Energy NEAMS (Nuclear Energy Advanced Modeling and Simulation) program. Los Alamos National Laboratory, an affirmative action/equal opportunity employer, is operated by Triad National Security LLC, for the National Nuclear Security Administration of the U.S. Department of Energy under Contract No. 89233218CNA000001.

References

[1] W. M. Armstrong, W. R. Irvine, and R. H. Martinson. Creep deformation of stoichiometric uranium dioxide. *Journal of Nuclear Materials*, 7(2):133–141, Nov 1962.

[2] B. Burton, G. L. Reynolds, and J. P. Barnes. The influence of grain size on the creep of uranium dioxide. *Journal of Materials Science*, 8(12):1690–1694, Dec 1973.

[3] B. Burton and G. L. Reynolds. The influence of deviations from stoichiometric composition on the diffusional creep of uranium dioxide. *Acta Metallurgica*, 21(12):1641–1647, Dec 1973.

[4] B. Burton and G. L. Reynolds. The diffusional creep of uranium dioxide: its limitation by interfacial processes. *Acta Metallurgica*, 21(8):1073–1078, Aug 1973.

[5] R. A. Wolfe and S. F. Kaufman. Mechanical properties of oxide fuels LSBR/LWB DEVELOPMENT PROGRAM. No. WAPD-TM-587. Technical report, Bettis Atomic Power Lab., Pittsburgh, PA (US), 1967.

[6] M. S. Seltzer, A. H. Clauer, and B. A. Wilcox. The stress dependence for high temperature creep of polycrystalline uranium dioxide. *Journal of Nuclear Materials*, 34(3):351–353, Mar 1970.

[7] T. E. Chung and T. J. Davies. The superplastic creep of uranium dioxide. *Journal of Nuclear Materials*, 79(1):143–153, Jan 1979.

[8] A. C. S. Sabioni, W. B. Ferraz, and F. Millot. First study of uranium self-diffusion in UO2 by SIMS. *Journal of Nuclear Materials*, 257(2):180–184, Nov 1998.

[9] P. Robbe, D. A. Andersson, L. Bonnet, T. A. Casey, M. W. D. Cooper, C. Matthews, K. Sargsyan, and H. N. Najm. Bayesian calibration with summary statistics for the prediction of xenon diffusion in UO2 nuclear fuel. *Computational Materials Science*, 225(April):112184, 2023.

[10] C. Duguay, A. Mocellin, Ph. Dehaudt, and G. Fantozzi. High Temperature Compression Tests Performed on Doped Fuels. *Key Engineering Materials*, 132-136:579–582, Apr 1997.

[11] D. A. Andersson, A. Rovinelli, L. Capolungo, C. O. T. Galvin, and M. W. D. Cooper. Incorporation of climb and the influence of grain boundary dopant concentration on UO2 creep. Technical report.

[12] C. M. Silva, R. D. Hunt, and K. S. Holliday. An evaluation of tri-valent oxide (Cr2O3) as a grain enlarging dopant for UO2 nuclear fuels fabricated under reducing environment. *Journal of Nuclear Materials*, 553:153053, Sep 2021.

[13] D. A. Andersson, C. R. Stanek, C. Matthews, and B. P. Uberuaga. The past, present, and future of nuclear fuel. *MRS Bulletin*, 48(11):1154–1162, Nov 2023.

[14] R. L. Williamson, J. D. Hales, S. R. Novascone, G. Pastore, K. A. Gamble, B. W. Spencer, W. Jiang, S. A. Pitts, A. Casagranda, D. Schwen, A. X. Zabriskie, A. Toptan, R. Gardner, C. Matthews, W. Liu, and H. Chen. BISON: A Flexible Code for Advanced Simulation of the Performance of Multiple Nuclear Fuel Forms. *Nuclear Technology*, 207(7):954–980, 2021.

[15] R. Sweet, L. Capolungo, C. O. T. Galvin, D. A. Andersson, and M. W. D. Cooper. Diffusional creep in UO2 informed by lower length scale simulations. Technical report.

[16] C. O. T. Galvin, D. A. Andersson, R. T. Sweet, L. Capolungo, and M. W. D. Cooper. Diffusional creep model in UO2 informed by lower-length scale simulations. *Journal of Nuclear Materials*, 607(January):155659, Mar 2025.

[17] P. E. Bohaboy, R. R. Asamoto, and A. E. Conti. Compressive Creep Characteristics of Stoichiometric Uranium Dioxide. *Other Information: UNCL. Orig. Receipt Date: 31-DEC-70*, (May), 1969.

[18] F. A. Mohamed and M. S. Soliman. On the creep behavior of uranium dioxide. *Materials Science and Engineering*, 53(2):185–190, May 1982.

[19] H. J. Frost and M. F. Ashby. Deformation-mechanism maps: the plasticity and creep of metals and ceramics. 1982.

[20] D. B. Knorr, R. M. Cannon, and R. L. Coble. Overview no. 84. *Acta Metallurgica*, 37(8):2103–2123, Aug 1989.

[21] O. A. Ruano, J. Wolfenstine, J. Wadsworth, and O. D. Sherby. Harper-Dorn and power law creep in uranium dioxide. *Acta Metallurgica et Materialia*, 39(4):661–668, Apr 1991.

[22] G. W. Greenwood. Denuded zones and diffusional creep. *Scripta Metallurgica et Materialia*, 30(12):1527–1530, Jun 1994.

[23] B. Burton and G. L. Reynolds. In defense of diffusional creep. *Materials Science and Engineering: A*, 191(1-2):135–141, Feb 1995.

[24] O. A. Ruano, O. D. Sherby, J. Wadsworth, and J. Wolfenstine. Rebuttal to "In defense of diffusional creep". *Materials Science and Engineering: A*, 211(1-2):66–71, Jun 1996.

[25] J. N. Wang and T. G. Nieh. A new interpretation of the mechanisms in Newtonian creep of uranium dioxides. *Journal of Nuclear Materials*, 228(1):141–147, Feb 1996.

[26] W. D. Neilson, C. O. T. Galvin, S. J. Dillon, M. W. D. Cooper, and D. A. Andersson. Irradiation-induced creep in UO2: The role of grain boundaries. *Physical Review Materials*, 8(10):103602, Oct 2024.

[27] A. Chakraborty, R. A. Lebensohn, and L. Capolungo. Coupled chemo-mechanical modeling of point-defect diffusion in a crystal plasticity fast Fourier transform framework. *Journal of the Mechanics and Physics of Solids*, 173:105190, Apr 2023.

[28] F. R. N. Nabarro. Report of a Conference on Strength of Solids. *Physical Society, London*, 75:590, 1948.

[29] C. Herring. Diffusional Viscosity of a Polycrystalline Solid. *Journal of Applied Physics*, 21(5):437–445, May 1950.

[30] R. L. Coble. A Model for Boundary Diffusion Controlled Creep in Polycrystalline Materials. *Journal of Applied Physics*, 34(6):1679–1682, Jun 1963.

[31] B. Dorado, D. A. Andersson, C. R. Stanek, M. Bertolus, B. P. Uberuaga, G. Martin, M. Freyss, and P. Garcia. First-principles calculations of uranium diffusion in uranium dioxide. *Physical Review B*, 86(3):035110, Jul 2012.

[32] C. Matthews, R. Perriot, M. W. D. Cooper, C. R. Stanek, and D. A. Andersson. Cluster dynamics simulation of uranium self-diffusion during irradiation in UO2. *Journal of Nuclear Materials*, 527:151787, Dec 2019.

[33] R. Perriot, C. Matthews, M. W. D. Cooper, B. P. Uberuaga, C. R. Stanek, and D. A. Andersson. Atomistic modeling of out-of-pile xenon diffusion by vacancy clusters in UO2. *Journal of Nuclear Materials*, 520:96–109, Jul 2019.

[34] J. Pelleg. *Creep in Ceramics*. Springer International Publishing, Cham, 2017.

[35] M. W. D. Cooper, K. A. Gamble, L. Capolungo, C. Matthews, D. A. Andersson, B. Beeler, C. R. Stanek, and K. Metzger. Irradiation-enhanced diffusion and diffusion-limited creep in U_3Si_2. *Journal of Nuclear Materials*, 555:153129, Nov 2021.

[36] H. Haario, E. Saksman, and J. Tamminen. An adaptive metropolis algorithm. *Bernoulli*, 7(2):223–242, 2001.

[37] G. E. P. Box and G. C. Tiao. *Bayesian Inference in Statistical Analysis*. John Wiley & Sons, 2011.

[38] T. Crestaux, O. Le Maître, and J.-M. Martinez. Polynomial chaos expansion for sensitivity analysis. *Reliability Engineering & System Safety*, 94(7):1161–1172, 2009.

[39] R. G. Ghanem and P. D. Spanos. *Stochastic Finite Elements: A Spectral Approach*. Courier Corporation, 2003.

[40] C. M. Bishop and N. M. Nasrabadi. *Pattern Recognition and Machine Learning*. Springer, 2006.

[41] D. P. Kingma and J. Ba. *Adam: A Method for Stochastic Optimization*. arXiv preprint arXiv:1412.6980, 2014.

[42] J. K. Joy, A. Rovinelli, M. Arul Kumar, R. A. Lebensohn, L. Capolungo, Q. Q. Ren, Y. Yamamoto, J. D. Poplawsky, M. Detrois, and P. Jablonski. Experimental and Numerical Characterization of High Temperature Deformation Behavior of 347H Stainless Steel. In *Proceedings*, pages 99–110, Oct 2024.

[43] W. Wen, A. Kohnert, M. Arul Kumar, L. Capolungo, and C. N. Tomé. Mechanism-based modeling of thermal and irradiation creep behavior: An application to ferritic/martensitic HT9 steel. *International Journal of Plasticity*, 126:102633, Mar 2020.

[44] T. Okita and W. G. Wolfer. A critical test of the classical rate theory for void swelling. *Journal of Nuclear Materials*, 327(2-3):130–139, May 2004.

[45] A. A. Kohnert, B. D. Wirth, and L. Capolungo. Modeling microstructural evolution in irradiated materials with cluster dynamics methods: A review. *Computational Materials Science*, 149:442–459, Jun 2018.

[46] L. Portelette, J. Amodeo, R. Madec, J. Soulacroix, T. Helfer, and B. Michel. Crystal viscoplastic modeling of UO2 single crystal. *Journal of Nuclear Materials*, 510:635–643, Nov 2018.

[47] L. Portelette, J. Amodeo, B. Michel, and R. Madec. Athermal dislocation strengthening in UO2. *Journal of Nuclear Materials*, 538:152157, Sep 2020.

[48] R. Madec, L. Portelette, B. Michel, and J. Amodeo. Plastic anisotropy and composite slip: Application to uranium dioxide. *Acta Materialia*, 255:119016, Aug 2023.

[49] W. M. Armstrong, A. R. Causey, and W. R. Sturrock. Creep of single-crystal UO2. *Journal of Nuclear Materials*, 19(1):42–49, Apr 1966.

[50] R. T. Sweet, J. A. Hirschhorn, C. O. T. Galvin, and S. R. Novascone. Improved simulation of UO2 fuel creep deformation in LWR fuel elements. *Transactions of the American Nuclear Society*, 130(1):505–508, 2024.

[51] S. J. Dillon, E. Lang, S. C. Finkeldei, J. Ouyang, and K. Hattar. A nucleation rate limited model for grain boundary creep. *Acta Materialia*, 246(December 2022):118718, mar 2023.

[52] D. R. Gaston, C. J. Permann, J. W. Peterson, A. E. Slaughter, D. Andrš, Y. Wang, M. P. Short, D. M. Perez, M. R. Tonks, J. Ortensi, L. Zou, and R. C. Martineau. Physics-based multiscale coupling for full core nuclear reactor simulation. *Annals of Nuclear Energy*, 84:45–54, 2015.

[53] M. R. Tonks, D. A. Andersson, S. R. Phillpot, Y. Zhang, R. Williamson, C. R. Stanek, B. P. Uberuaga, and S. L. Hayes. Mechanistic materials modeling for nuclear fuel performance. *Annals of Nuclear Energy*, 105:11–24, Jul 2017.

[54] P. Garcia, A. Miard, T. Helfer, J.-B. Parise, X. Iltis, and G. Antou. The effect of oxygen partial pressure on dislocation creep in polycrystalline uranium dioxide. *Journal of the European Ceramic Society*, 41(3):2124–2133, Mar 2021.

[55] C. Matthews, R. Perriot, M. W. D. Cooper, C. R. Stanek, and D. A. Andersson. Cluster dynamics simulation of xenon diffusion during irradiation in UO2. *Journal of Nuclear Materials*, 540:152326, Nov 2020.

[56] C. Matthews, M. W. D. Cooper, P. Robbe, T. Casey, K. Sargsyan, H. N. Najm, G. Pastore, S. Blondel, N. Militello, B. Wirth, A. Levinsky, J. White, T. Gibson, C. R. Stanek, and D. A. Andersson. Mechanistic multiscale uncertainty propagation in support of accelerated fuel qualification. *ANS Special Issue*.

[57] J. A. Vrugt and C. J. F. Ter Braak. DREAM(D): An adaptive Markov Chain Monte Carlo simulation algorithm to solve discrete, noncontinuous, and combinatorial posterior parameter estimation problems. *Hydrology and Earth System Sciences*, 15(12):3701–3713, Dec 2011.

[58] M. D. Hoffman and A. Gelman. The No-U-Turn Sampler: Adaptively Setting Path Lengths in Hamiltonian Monte Carlo. *Journal of Machine Learning Research*, 15:1593–1623, 2011.

[59] A. Doucet, N. Freitas, and N. Gordon. An Introduction to Sequential Monte Carlo Methods. In *Sequential Monte Carlo Methods in Practice*, pages 3–14, 2001.

[60] C. Guéneau, A. Chartier, and L. Van Brutzel. Thermodynamic and Thermophysical Properties of the Actinide Oxides. In *Comprehensive Nuclear Materials*, volume 2, pages 21–59. Elsevier, 2012.

[61] C. A. Butler, A. Nichols, J. T. White, and S. W. Paisner. Status report on the thermomechanical properties testing of Cr-doped UO2. Technical report.

Appendix

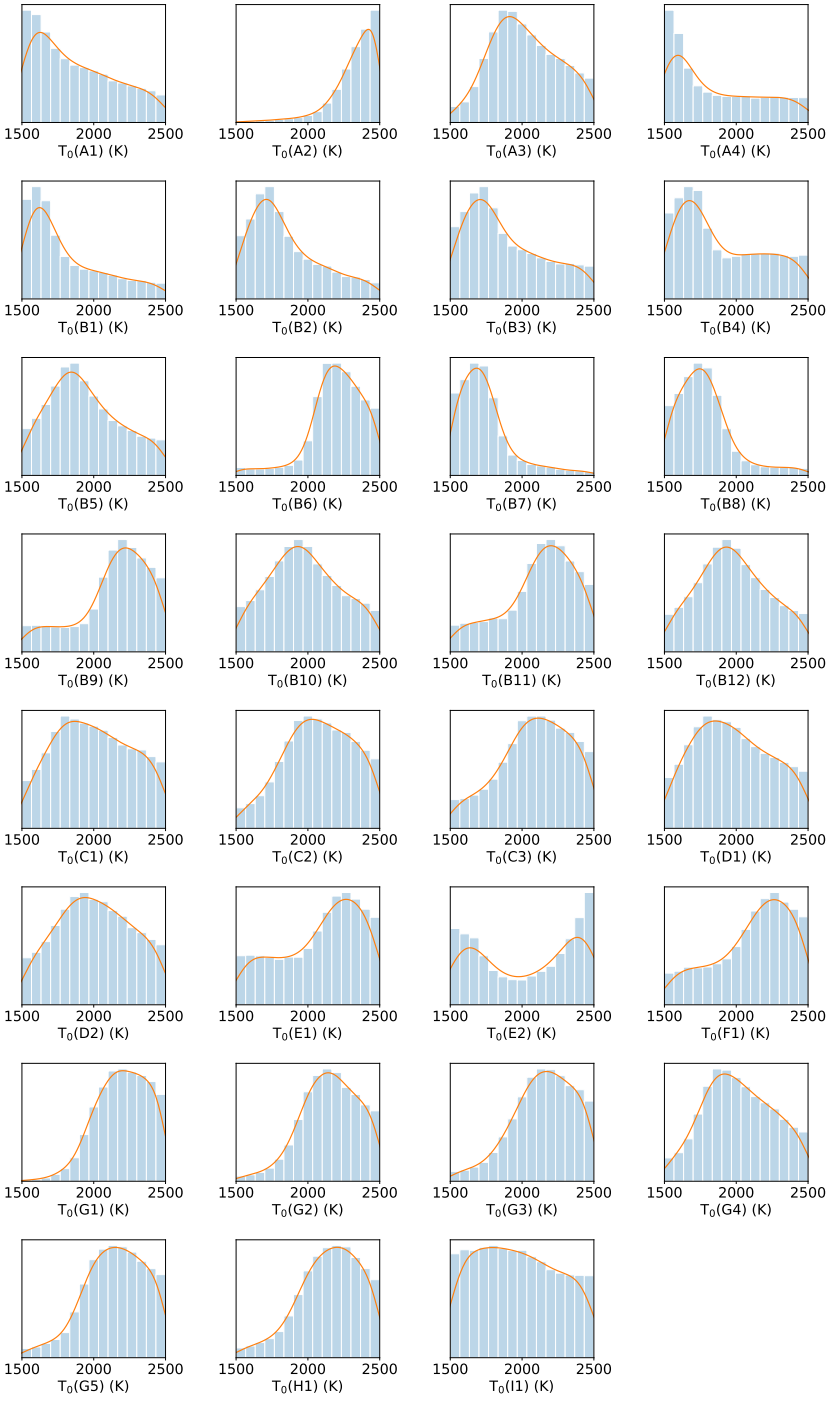

Figure A1: Posterior distributions for all T_0 model parameters. See Table A1 for reference index to experiment.

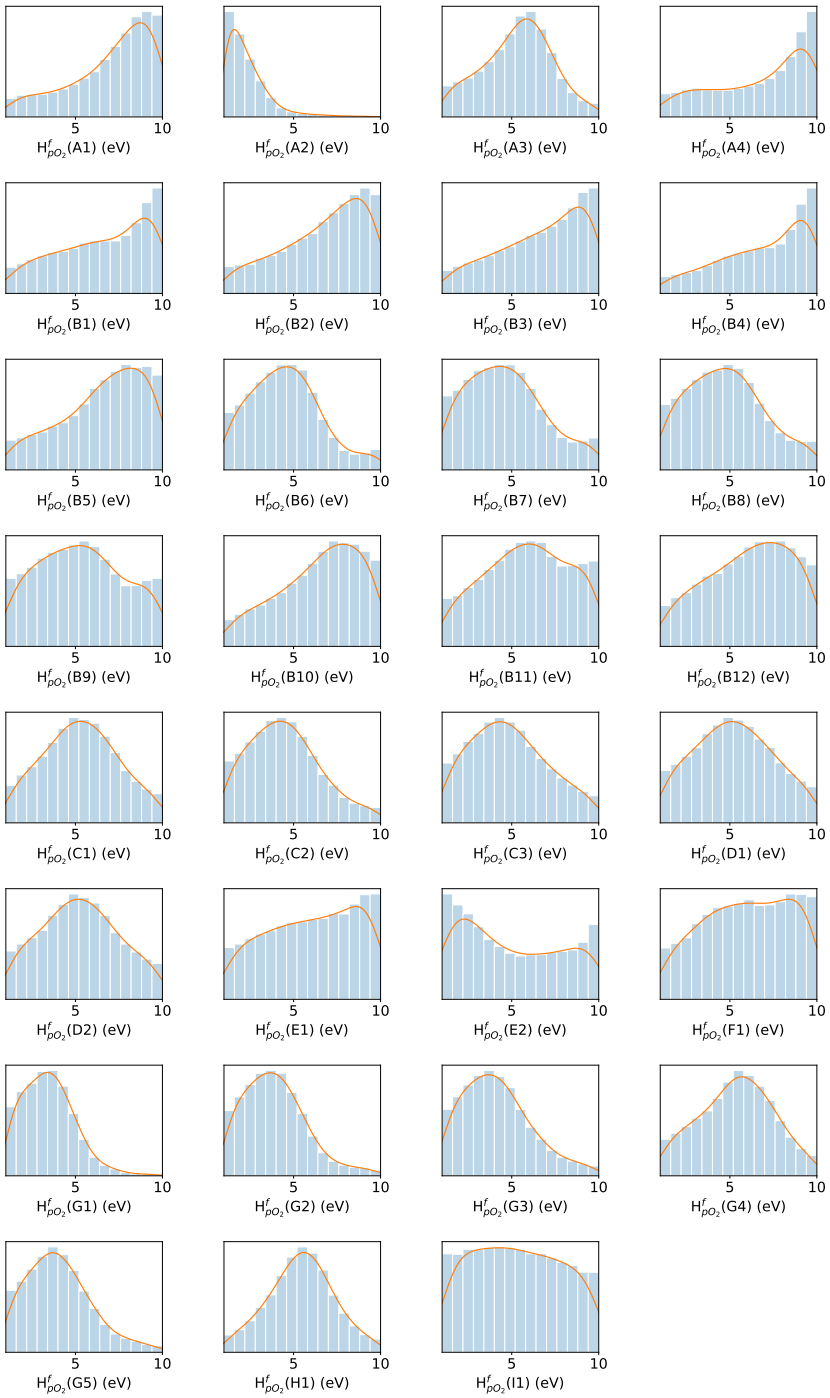

Figure A2: Posterior distributions for all H_{fpO_2} model parameters. See Table A1 for reference index to experiment.

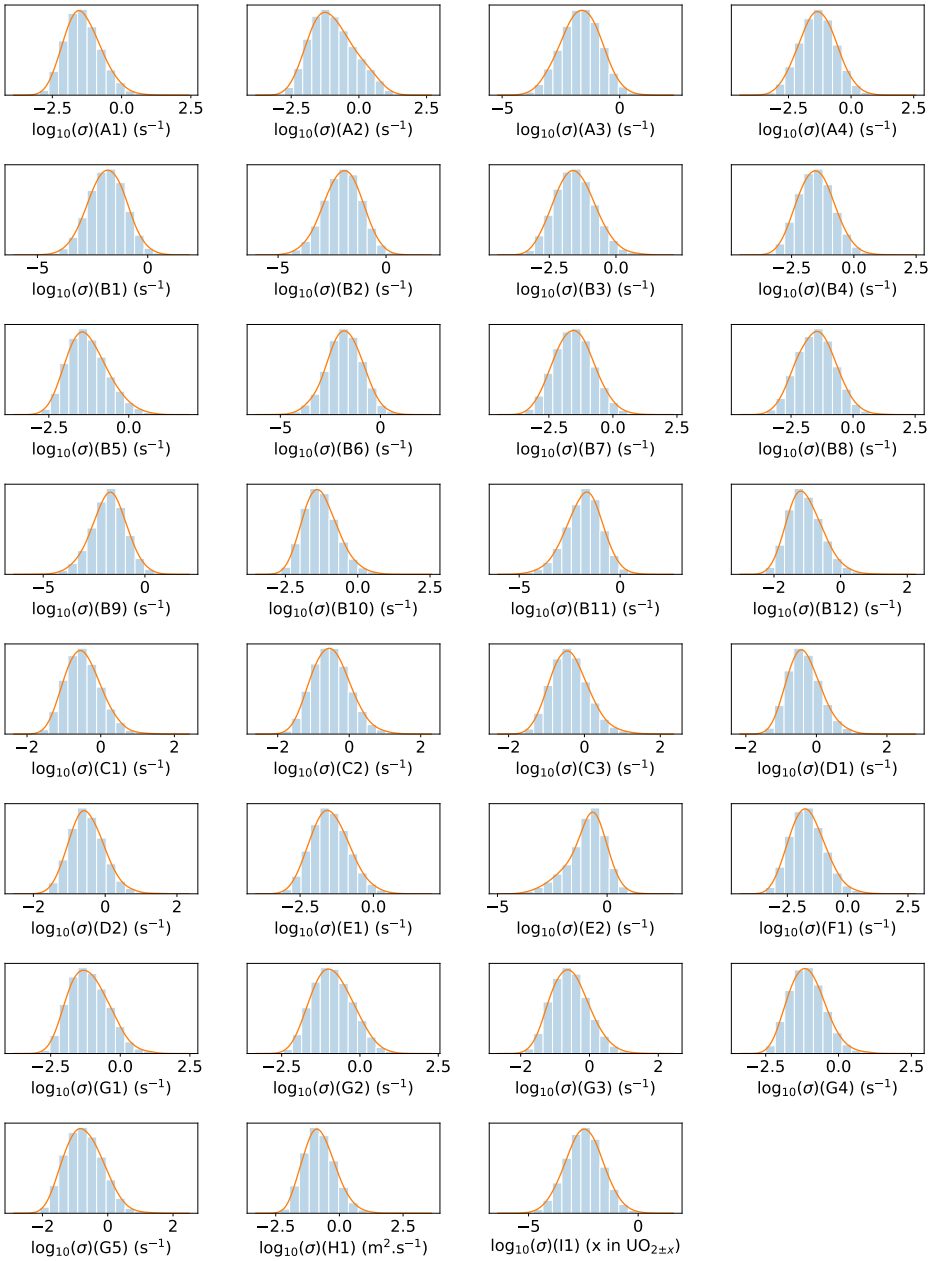

Figure A3: Inferred standard deviation of the Gaussian noise distributions of the likelihood function, which describes the experimental measurement scattering as well as the difference between modeling and experimental results.

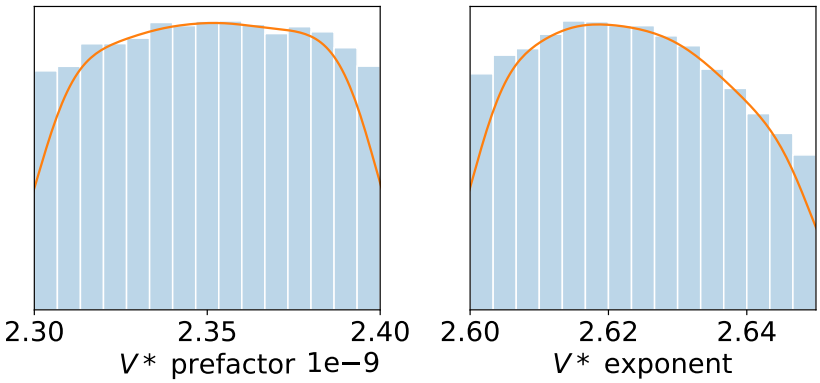

Figure A4: Posterior distributions for model parameters. See Table A1 for reference index to experiment.

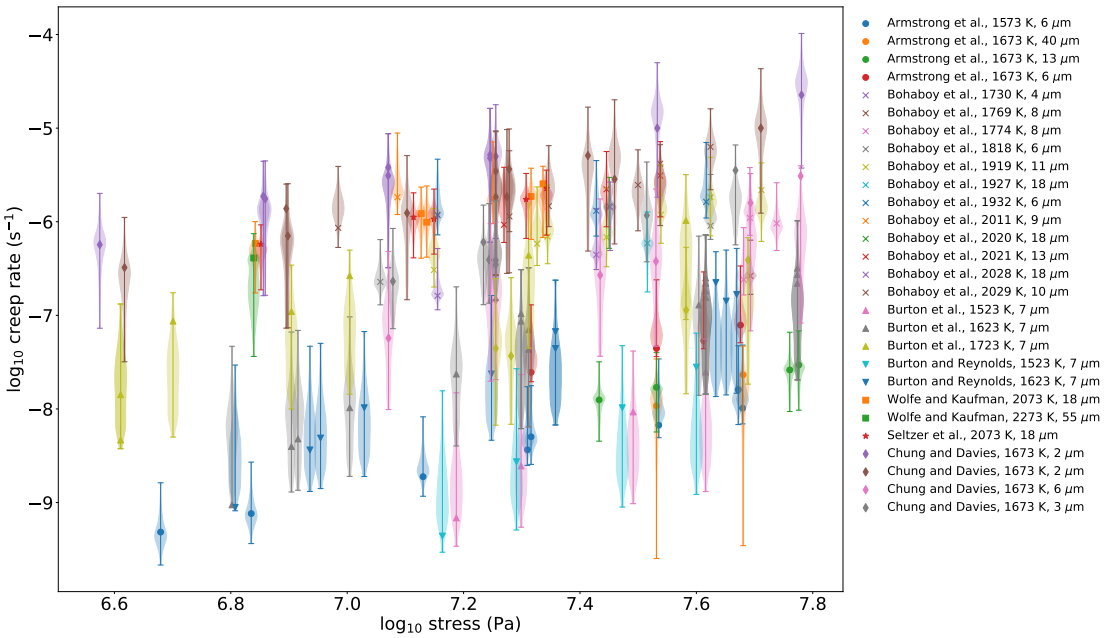

Figure A5: Pushforward posterior distributions for creep rate as a function of stress for all experiments considered.

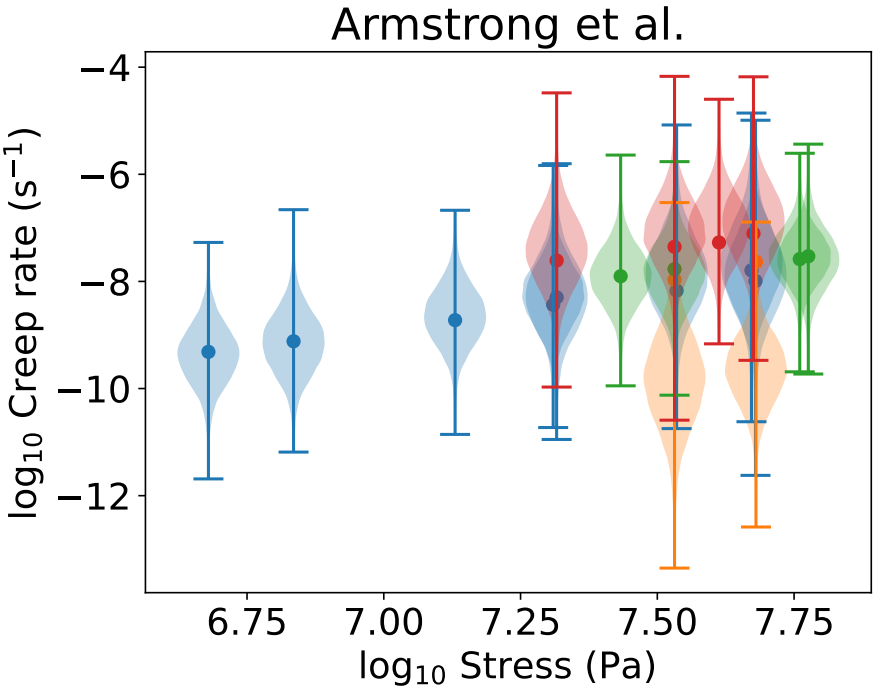

(a) Experimental data [1]

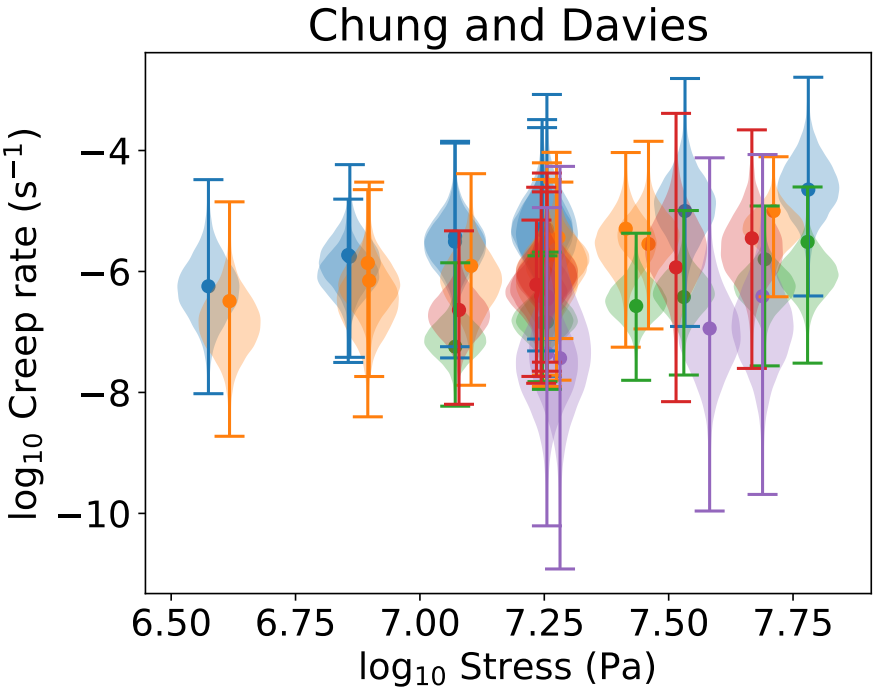

(b) Experimental data [7]

Figure A6: Posterior predictive distributions for creep rate as a function of stress. They encapsulate the pushforward posterior distributions and the Gaussian noise of the likelihood function.

Table A1: Table for all creep experiments and conditions considered in this study. Refer to [9] for uranium bulk self-diffusivity and non-stoichiometry conditions.

Temp (K)	Grain (m)	Stress (MPa)	Creep rate exp ($s^{-}1$)	Study	Experiment
1573.15	6.00E-06	4.78	4.84E-10	Armstrong et al.	A1
1573.15	6.00E-06	6.84	7.63E-10	Armstrong et al.	A1
1573.15	6.00E-06	13.50	1.89E-09	Armstrong et al.	A1
1573.15	6.00E-06	20.40	3.66E-09	Armstrong et al.	A1
1573.15	6.00E-06	20.70	5.04E-09	Armstrong et al.	A1
1573.15	6.00E-06	34.30	6.71E-09	Armstrong et al.	A1
1573.15	6.00E-06	47.80	1.02E-08	Armstrong et al.	A1
1573.15	6.00E-06	47.00	1.61E-08	Armstrong et al.	A1
1673.15	4.00E-05	34.00	1.08E-08	Armstrong et al.	A2
1673.15	4.00E-05	47.90	2.32E-08	Armstrong et al.	A2
1673.15	1.30E-05	27.10	1.25E-08	Armstrong et al.	A3
1673.15	1.30E-05	34.00	1.70E-08	Armstrong et al.	A3
1673.15	1.30E-05	57.60	2.61E-08	Armstrong et al.	A3
1673.15	1.30E-05	59.70	2.95E-08	Armstrong et al.	A3
1673.15	6.00E-06	20.70	2.46E-08	Armstrong et al.	A4
1673.15	6.00E-06	34.00	4.43E-08	Armstrong et al.	A4
1673.15	6.00E-06	41.00	5.33E-08	Armstrong et al.	A4
1673.15	6.00E-06	47.40	7.86E-08	Armstrong et al.	A4
1730	4.00E-06	26.80	4.44E-07	Bohaboy et al.	B1
1731	4.00E-06	14.30	1.62E-07	Bohaboy et al.	B1
1769	8.00E-06	49.30	2.64E-07	Bohaboy et al.	B2
1774	8.00E-06	48.00	2.41E-07	Bohaboy et al.	B3
1812	7.00E-06	54.70	9.61E-07	Bohaboy et al.	B3
1813	6.00E-06	49.20	1.10E-06	Bohaboy et al.	B3
1818	6.00E-06	42.10	9.06E-07	Bohaboy et al.	B4
1825	6.00E-06	11.40	2.28E-07	Bohaboy et al.	B4
1919	1.10E-05	27.90	6.83E-07	Bohaboy et al.	B5
1920	1.00E-05	14.10	3.06E-07	Bohaboy et al.	B5
1920	1.10E-05	51.50	2.18E-06	Bohaboy et al.	B5
1922	1.00E-05	21.20	5.83E-07	Bohaboy et al.	B5
1922	1.00E-05	22.10	6.94E-07	Bohaboy et al.	B5
1924	1.00E-05	42.10	1.83E-06	Bohaboy et al.	B5
1925	1.00E-05	34.60	1.19E-06	Bohaboy et al.	B5
1927	1.80E-05	32.80	5.89E-07	Bohaboy et al.	B6
1932	6.00E-06	14.30	1.00E-06	Bohaboy et al.	B7
1932	8.00E-06	26.80	1.00E-06	Bohaboy et al.	B7
1932	8.00E-06	41.40	2.00E-06	Bohaboy et al.	B7
2011	9.00E-06	17.80	2.00E-06	Bohaboy et al.	B8
2012	7.00E-06	12.20	2.00E-06	Bohaboy et al.	B8
2020	1.80E-05	28.20	1.00E-06	Bohaboy et al.	B9

Temp (K)	Grain (m)	Stress (MPa)	Creep rate exp ($s^{-}1$)	Study	Experiment
2021	1.30E-05	27.90	2.22E-06	Bohaboy et al.	B10
2024	1.30E-05	18.60	9.28E-07	Bohaboy et al.	B10
2024	1.30E-05	34.50	3.11E-06	Bohaboy et al.	B10
2028	1.80E-05	28.30	1.00E-06	Bohaboy et al.	B11
2029	1.00E-05	9.65	8.61E-07	Bohaboy et al.	B12
2029	1.20E-05	22.20	1.47E-06	Bohaboy et al.	B12
2029	1.40E-05	31.60	2.47E-06	Bohaboy et al.	B12
2029	1.10E-05	42.10	6.31E-06	Bohaboy et al.	B12
2033	1.20E-05	19.00	1.14E-06	Bohaboy et al.	B12
2033	1.40E-05	34.50	4.17E-06	Bohaboy et al.	B12
1523	7.00E-06	15.40	6.86E-10	Burton et al.	C1
1523	7.00E-06	19.90	2.46E-09	Burton et al.	C1
1523	7.00E-06	31.00	9.29E-09	Burton et al.	C1
1523	7.00E-06	41.30	2.48E-08	Burton et al.	C1
1623	7.00E-06	6.34	9.44E-10	Burton et al.	C2
1623	7.00E-06	8.02	3.97E-09	Burton et al.	C2
1623	7.00E-06	8.23	4.78E-09	Burton et al.	C2
1623	7.00E-06	10.10	1.03E-08	Burton et al.	C2
1623	7.00E-06	15.40	2.36E-08	Burton et al.	C2
1623	7.00E-06	20.50	4.34E-08	Burton et al.	C2
1623	7.00E-06	20.50	7.01E-08	Burton et al.	C2
1623	7.00E-06	19.90	8.67E-08	Burton et al.	C2
1623	7.00E-06	19.90	1.04E-07	Burton et al.	C2
1623	7.00E-06	40.20	1.29E-07	Burton et al.	C2
1623	7.00E-06	41.30	1.56E-07	Burton et al.	C2
1623	7.00E-06	41.30	1.82E-07	Burton et al.	C2
1623	7.00E-06	41.30	2.20E-07	Burton et al.	C2
1623	7.00E-06	41.30	2.51E-07	Burton et al.	C2
1623	7.00E-06	59.40	2.20E-07	Burton et al.	C2
1623	7.00E-06	59.40	2.72E-07	Burton et al.	C2
1623	7.00E-06	59.40	3.19E-07	Burton et al.	C2
1723	7.00E-06	4.08	4.65E-09	Burton et al.	C3
1723	7.00E-06	4.08	1.42E-08	Burton et al.	C3
1723	7.00E-06	5.02	8.67E-08	Burton et al.	C3
1723	7.00E-06	8.02	1.10E-07	Burton et al.	C3
1723	7.00E-06	10.10	2.65E-07	Burton et al.	C3
1723	7.00E-06	20.50	4.39E-07	Burton et al.	C3
1723	7.00E-06	38.20	1.03E-06	Burton et al.	C3
1523	7.00E-06	14.58	4.39E-10	Burton and Reynolds	D1
1523	7.00E-06	19.54	2.73E-09	Burton and Reynolds	D1
1523	7.00E-06	29.70	1.03E-08	Burton and Reynolds	D1
1523	7.00E-06	39.81	2.80E-08	Burton and Reynolds	D1
1623	7.00E-06	6.42	8.89E-10	Burton and Reynolds	D2

Temp (K)	Grain (m)	Stress (MPa)	Creep rate exp ($s^{-}1$)	Study	Experiment
1623	7.00E-06	8.63	3.65E-09	Burton and Reynolds	D2
1623	7.00E-06	9.00	4.89E-09	Burton and Reynolds	D2
1623	7.00E-06	10.70	1.03E-08	Burton and Reynolds	D2
1623	7.00E-06	17.70	2.37E-08	Burton and Reynolds	D2
1623	7.00E-06	22.80	4.42E-08	Burton and Reynolds	D2
1623	7.00E-06	22.80	6.70E-08	Burton and Reynolds	D2
1623	7.00E-06	44.80	1.42E-07	Burton and Reynolds	D2
1623	7.00E-06	46.70	1.67E-07	Burton and Reynolds	D2
1623	7.00E-06	43.00	2.24E-07	Burton and Reynolds	D2
2073.15	1.80E-05	6.95	5.87E-07	Wolfe and Kaufman	E1
2073.15	1.80E-05	13.40	1.22E-06	Wolfe and Kaufman	E1
2073.15	1.80E-05	13.70	9.90E-07	Wolfe and Kaufman	E1
2073.15	1.80E-05	20.70	1.86E-06	Wolfe and Kaufman	E1
2073.15	1.80E-05	21.70	2.54E-06	Wolfe and Kaufman	E1
2273.15	5.50E-05	6.91	4.10E-07	Wolfe and Kaufman	E2
2073.15	1.80E-05	7.11	5.76E-07	Seltzer et al.	F1
2073.15	1.80E-05	13.00	1.12E-06	Seltzer et al.	F1
2073.15	1.80E-05	14.10	1.07E-06	Seltzer et al.	F1
2073.15	1.80E-05	20.30	1.73E-06	Seltzer et al.	F1
2073.15	1.80E-05	22.00	2.27E-06	Seltzer et al.	F1
1673	2.00E-06	3.76	5.69E-07	Chung and Davies	G1
1673	2.00E-06	7.18	1.87E-06	Chung and Davies	G1
1673	2.00E-06	7.23	1.76E-06	Chung and Davies	G1
1673	2.00E-06	11.80	3.11E-06	Chung and Davies	G1
1673	2.00E-06	11.80	3.80E-06	Chung and Davies	G1
1673	2.00E-06	17.60	4.78E-06	Chung and Davies	G1
1673	2.00E-06	17.60	5.17E-06	Chung and Davies	G1
1673	2.00E-06	18.00	4.99E-06	Chung and Davies	G1
1673	2.00E-06	34.10	1.00E-05	Chung and Davies	G1
1673	2.00E-06	60.30	2.26E-05	Chung and Davies	G1
1673	3.00E-06	4.14	3.24E-07	Chung and Davies	G2
1673	3.00E-06	7.86	1.38E-06	Chung and Davies	G2
1673	3.00E-06	7.91	7.06E-07	Chung and Davies	G2
1673	3.00E-06	12.70	1.24E-06	Chung and Davies	G2
1673	2.00E-06	18.00	1.84E-06	Chung and Davies	G2
1673	2.00E-06	18.00	3.46E-06	Chung and Davies	G2
1673	3.00E-06	18.80	1.85E-06	Chung and Davies	G2
1673	3.00E-06	19.00	3.65E-06	Chung and Davies	G2
1673	3.00E-06	25.90	5.09E-06	Chung and Davies	G2
1673	3.00E-06	28.80	2.85E-06	Chung and Davies	G2
1673	3.00E-06	51.40	1.00E-05	Chung and Davies	G2
1673	6.00E-06	11.78	5.71E-08	Chung and Davies	G3
1673	6.00E-06	17.63	1.43E-07	Chung and Davies	G3

Temp (K)	Grain (m)	Stress (MPa)	Creep rate exp (s^-1)	Study	Experiment
1673	6.00E-06	18.00	1.46E-07	Chung and Davies	G3
1673	6.00E-06	27.21	2.69E-07	Chung and Davies	G3
1673	6.00E-06	33.92	3.78E-07	Chung and Davies	G3
1673	6.00E-06	49.32	1.59E-06	Chung and Davies	G3
1673	6.00E-06	60.15	3.08E-06	Chung and Davies	G3
1673	3.00E-06	11.98	2.31E-07	Chung and Davies	G4
1673	3.00E-06	17.15	6.05E-07	Chung and Davies	G4
1673	3.00E-06	17.53	3.93E-07	Chung and Davies	G4
1673	3.00E-06	18.00	3.88E-07	Chung and Davies	G4
1673	3.00E-06	18.00	3.48E-07	Chung and Davies	G4
1673	3.00E-06	32.72	1.17E-06	Chung and Davies	G4
1673	3.00E-06	46.48	3.54E-06	Chung and Davies	G4
1673	1.00E-05	18.00	4.44E-08	Chung and Davies	G5
1673	1.00E-05	19.13	3.68E-08	Chung and Davies	G5
1673	1.00E-05	38.23	1.14E-07	Chung and Davies	G5
1673	1.00E-05	48.84	3.90E-07	Chung and Davies	G5

Table A2: Table showing nominal, prior and the most probable values. Refer to [9] and [26] for other nominal values.

Parameters	Nominal	Lower bound	Upper bound	Most probable value
H_{UO_2}	-3435.26	-3435.51	-3435.01	-3435.48
H_{V_U}	-3381.04	-3381.29	-3380.79	-3381.20
H_h	-3444.05	-3444.30	-3443.80	-3443.90
H_{O_i}	-3423.45	-3423.70	-3423.20	-3423.52
S_{UO_2}	-129368.83	-129371.33	-129366.33	-129370.65
S_{O_i}	-129445.29	-129447.79	-129442.79	-129445.20
T_0	2373.00	1500.00	2500.00	-
$H^f_{pO_2}$	5.90	1.00	10.00	-
$log_{10}D_0^{V_U,GB}$	-3.82	-4.82	-1.82	-1.93
$H^m_{V_U,GB}$	2.71	1.71	3.71	2.21
$H^{seg}_{V_U}$	-3.21	-4.21	-2.21	-2.47
$H^{seg}_{V_O}$	-1.35	-2.35	-0.35	-0.40
$\nu^* prefactor$	2.37×10^{-9}	2.3×10^{-9}	2.4×10^{-9}	2.35×10^{-9}
$\nu^* exponent$	2.63	2.6	2.65	2.62